Electronic Supplementary Material (ESI) for Energy & Environmental Science.

Electronic Supplementary Information

The synergistic catalysis effect on electrochemical nitrate reduction at the dual−function active sites of heterostructure

Yuxiang Li[a], Zhenjie Lu[b], Lei Zheng[c], Xing Yan[a], Junliang Xie[a], Zhonghao Yu[a], Shengli Zhang[c], Fang Jiang[a*], Huan Chen[a*]

[a] Key Laboratory of Jiangsu Province for Chemical Pollution Control and Resources Reuse, School of Environmental and Biological Engineering, Nanjing University of Science and Technology, Nanjing 210094, People's Republic of China.

*E−mail: fjiang@njust.edu.cn, hchen404@njust.edu.cn

[b] Key Laboratory for Soft Chemistry and Functional Materials of Ministry of Education, Nanjing University of Science and Technology, Nanjing 210094, China

[c] MIIT Key Laboratory of Advanced Display Materials & Devices, College of Material Science and Engineering, Nanjing University of Science and Technology, Nanjing 210094, China

1. Experimental section

1.1 Chemicals

The ammonium persulfate ($(NH_4)_2S_2O_8$), 2−methylimidazole ($C_4H_6N_2$), cobaltous nitrate hexahydrate ($Co(NO_3)_2·6H_2O$), and sodium hypophosphite (NaH_2PO_2) were purchased from Aladdin. The sodium hydroxide (NaOH), potassium hydroxide (KOH), potassium nitrite (KNO_2), potassium nitrate (KNO_3), ammonium chloride (NH_4Cl), and hydrazine standard solution (N_2H_4, 1000 ppm in 1.0 mol L^{-1} HCl) were purchased from Meryer. The ultrapure water (18 MΩ cm at 25 °C) was used for the preparation of all the standard solutions and electrolytes.

1.2 Catalysts preparation

Preparation of $Cu(OH)_2$/CF: Before the preparation of material, the CF should be pre−processed by sonic cleaning in dilute hydrochloric acid, acetone, and ethanol for several minutes, respectively. Typically, 1 g NaOH and 296 mg $(NH_4)_2S_2O_8$ were orderly dissolved in 10 mL H_2O under vigorous stirring until the solution became clear and transparent. A piece of 1 × 1 cm^2 pre−processed CF was immersed in the above solution for 10 min. Due to wet chemical oxidation, $Cu(OH)_2$ nanoneedle arrays uniformly grew over the CF. The light blue sample was cleaned three times with water and then placed in vacuum oven over night to obtain $Cu(OH)_2$/CF.

Preparation of CoP/C@Cu_3P/CF: Initially, 291 mg $Co(NO_3)_2·6H_2O$ was completely dissolved in 25 mL methanol to obtain solution A. Meanwhile, 800 mg $C_4H_6N_2$ was completely dissolved in 25 mL methanol to obtain solution B. Subsequently, $Cu(OH)_2$/CF was immersed in solution A for cation exchange. After aging for 48 h at room temperature, solution B was added to solution A containing $Cu(OH)_2$/CF. Once again, the mixture reacted for 2 h at room temperature. Eventually, the purple sample was taken out and then ultrasonically cleaned three times using methanol. ZIF−67@ $Cu(OH)_2$/CF was obtained through drying in a vacuum oven over night.

CoP/C@Cu_3P/CF was synthesized via one−step phosphorization of ZIF−67@ $Cu(OH)_2$/CF. Specifically, the NaH_2PO_2 powder and ZIF−67@ $Cu(OH)_2$/CF were put at the gas flow upstream side and center of tube furnace, respectively. In the process of temperature programming, the sample was heated at 300 °C for 2 h with a heating rate of 2 °C /min under N_2 atmosphere. After naturally cooling to ambient temperature, the final sample was collected from crucible and marked as p−CoP/C@Cu_3P/CF (poor, 1:2), o−CoP/C@Cu_3P/CF (optimal, 1:1), and e−CoP/C@ Cu_3P/CF (excess, 3:1) according to the mass ratios of NaH_2PO_2 and ZIF−67@ $Cu(OH)_2$/CF.

The separated CoP/C@Cu_3P was obtained by the ultrasonic treatment of CoP/C@Cu_3P/CF.

Preparation of Cu_3P/CF: Cu_3P/CF was synthesized under the same phosphorization conditions as o−CoP/C@Cu_3P/CF, while the precursor was $Cu(OH)_2$/CF.

Preparation of CoP/C@CF: ZIF−67@CF was synthesized under the same experimental conditions as ZIF−67@ $Cu(OH)_2$/CF, while the precursor was CF. To obtain CoP/C@ CF, it's necessary for ZIF−67@CF to proceed the same phosphorization conditions as o−CoP/C@Cu_3P/CF.

Preparation of CoP/C_{powder}@CF and CN_{powder}@CF: CoP/C_{powder} was synthesized under the same phosphorization conditions as o−CoP/C@Cu_3P/CF, while the precursor was ZIF−67_{powder}. CN_{powder} was obtained by the acid treatment of ZIF−$67_{powder.}$ Subsequently, CoP/C_{powder}@CF and CN_{powder}@CF were obtained by dropping−coating the CoP/C_{powder} and CN_{powder} on CF, respectively.

1.3 Characterization

The crystal structures of the obtained samples were proved by XRD (Smartlab XRD) at the scan rate of 5°min^{-1} (Cu−Kα radiation at 40 kV and 40 mA, $\lambda = 0.15418$ nm). The information of Raman spectra was measured by LabRAM Aramis (HORIBA JOBIN YVON, France). The SEM (JSM−7800F PRIME), and HAADF−STEM (FEI Tecnai G2 F20) were carried out to obtain the morphology and microstructure of all samples. The chemical composition and valence state of all samples were analyzed by XPS (Thermo Scientific K−Alpha). Nuclear magnetic resonance (NMR) spectra were detected on an Avance Ⅲ 500 MHz. Ultraviolet−visible spectroscopy (UV−vis) was determined by UV−5500 PC. Electron paramagnetic resonance (EPR) spectra were recorded on a EMXplus−9./12 spectrometer using DMPO as the *H spin trapping reagent. In situ attenuated total reflectance−surface enhanced infrared absorption spectra (ATR−SEIRAS) was executed by the Nicolet iS50 FTIR spectrometer equipped with MCT detector and reflectance unit for the electrochemical cell at an incidence angle of 60°. The electrocatalyst ink was dropped on the silicon crystal covered with Au membrane and then dried in air before testing. To obtain stable signal, the detector should be cooled with liquid nitrogen for at least 30 min. In situ shell−isolated nanoparticle enhanced Raman spectra (SHINERS) was measured by LabRAM HR Evolution (HORIBA Jobin Yvon) Raman spectrometer. The excitation wavelength of the laser was 532 nm. The electrode modified by SHIN (50 nm Au@ 5~10 nm SiO_2) was placed in an electrochemical cell with 1 M KOH + 0.1 M KNO_3 electrolyte.

1.4 Electrochemical nitrate reduction measurements

The electrochemical nitrate reduction reaction (NITRR) experiment was executed in H−type cell, containing 40 mL cathode and anode electrolyte (1 M KOH + 0.1 M KNO_3), respectively. Specifically, a standard three−electrode system separated by Nafion 117 proton exchange membrane, which was connected to the working electrode, Hg/HgO reference electrode (1 M KOH), and platinum (Pt) counter electrode through electrochemical workstation (CHI 660E). The Nafion 117 membrane was pretreated by heating in H_2O_2 aqueous (5wt%) solution, 0.5 M H_2SO_4 and DI at 80°C for 1h, respectively. More importantly, the electrolyte should be purged with Ar for at least 30 min before electrolysis. The acid trap (0.05 M H_2SO_4) was employed to collect the volatile ammonia. The prepared working electrode should be pre−activated by cyclic voltammetry (CV) and chronoamperometry (CA) for 30 min, respectively. The linear sweep voltammetry (LSV) was executed with a rate of 20 mV s^{-1} from +0.3 to −0.4 V *vs. RHE*. The NITRR test was carried out using CA at various potentials for 1 h. All potentials were converted to the reversible hydrogen electrode (*RHE*) potentials via the Nernst equation: $E\ (vs.\ RHE) = E\ (vs.\ Hg/HgO) + 0.059 \times pH + 0.098$.

1.5 Determination of ammonia

The concentration of produced NH_3 after electrolysis was quantified by indophenol blue method.[1] In detail, 2 mL of diluted cathode electrolyte was followed by sequential addition of 1 M NaOH solution containing 5 wt% salicylic acid and 5 wt% sodium citrate (2 mL), 0.05 M NaClO solution (1 mL) and 1 wt% $C_5FeN_6Na_2O$ solution (0.2 mL). After the incubation for 1 h under ambient condition, the absorption spectrum ranging from at 500 nm to 800 nm of resulted solution was measured using UV−vis Spectrophotometer. The concentration−absorption curve was calibrated by a series of NH_4Cl gradient concentrations (0.0, 0.5, 1.0, 1.5, 2.0 and 4.0 μg/mL of NH_3) in 1 M KOH + 0.1 M KNO_3 electrolyte. The fitting curve presented good linear relationship, which was used to calculate the concentration of NH_3 in electrolyte.

1.6 Determination of nitrite

The concentration of produced NO_2^- after electrolysis was quantified by Griess reagent consisting of N−(1−naphthyl)ethyl−enediamine dihydrochloride (0.2 g), sulfanilamide (4 g), H_3PO_4 (10 mL), and H_2O (50 mL).[2] In detail, 2 mL diluted cathode electrolyte was mixed with 0.1 mL as−prepared color reagent. After the incubation for 20 min under ambient condition, the absorption spectrum ranging from at 400 nm to 700 nm of resulted solution was measured using UV−vis Spectrophotometer. The concentration−absorption curve was calibrated by a series of standard NO_2^- gradient concentrations (0.0, 0.4, 0.8, 1.2, 1.6 and 2.0 μg/mL of NO_2^-) in 1 M KOH + 0.1 M KNO_3 electrolyte. The fitting curve presented good linear relationship, which was used to calculate the concentration of NO_2^- in electrolyte.

1.7 Determination of hydrazine

The concentration of produced N_2H_4 after electrolysis was quantified by Watt and Chrisp method with the color reagent consisting of para−(dimenthylamino) benzaldehyde (5.99 g), HCl (30 mL), and ethanol (300 mL).[3] In detail, 2 mL cathode electrolyte was mixed with 2 mL as−prepared color reagent. After the incubation for 20 min under ambient condition, the absorption spectrum ranging from at 410 nm to 510 nm of resulted solution was measured using UV−vis Spectrophotometer. The concentration−absorption curve was calibrated by a series of standard N_2H_4 gradient concentrations (0.0, 0.4, 0.8, 1.2, 1.6 and 2.0 μg/mL of N_2H_4) in 1 M KOH + 0.1 M KNO_3 electrolyte. The fitting curve presented good linear relationship, which was used to calculate the concentration of N_2H_4 in electrolyte.

1.8 ^{1}H Nuclear magnetic resonance quantitative experiment

The KNO_3 was used as the feeding N−source for the nitrate reduction experiments to clarify the source of ammonia. The CA test was executed in the electrolyte containing 1 M KOH and 0.1 M KNO_3. After electrolysis, the cathode electrolyte containing NH_4^+ was taken out and adjusted to acidity with 4 M H_2SO_4 for further quantification by ^1H NMR (500 MHz) with internal standard of maleic acid.

The NH_3 calibration curve was obtained as follows. First, a series of NH_4Cl solutions with known concentrations (0, 200, 400, 600, 800, 1000 μg/mL of NH_3) were prepared in 1 M KOH as standard. Second, 5 mL NH_3 standard solution with different concentration mixed with 1 mL of 4 M H_2SO_4 and 2.5 mg of maleic acid. Third, 50 μL d6−DMSO was added in 0.5 mL above mixed solution for the NMR detection. Fourth, the calibration was achieved using the peak area ratio between NH_4^+ and maleic acid, because the NH_3 concentration and the area ratio were positively correlated.

1.9 The yield rate and Faradaic efficiency of ammonia

The NH_3 yield $r(NH_3)$ rate was calculated by the following equation:

$$r(NH_3) = \frac{C_{NH_3} \times V}{t \times A}$$

The Faradaic efficiency $FE(NH_3)$ referred to the percentage of the electric charge used for NITRR compared to the total electric charge, which can be obtained by the following equation:

$$FE(NH_3) = \frac{Q_{NH_3}}{Q_{total}} = \frac{8F \times C_{NH_3} \times V}{17Q} \times 100\%$$

Where C_{NH_3} is the measured concentration of NH_3, V is the volume of the cathode electrolyte (40 mL), t is the reaction time (1 h), A is the area of working electrode (1×1 cm^2), F is the Faraday constant (96,485 C mol^{-1}), and Q is the integration of i−t curve electric charge during the NITRR chronoamperometry test.

1.10 Computational details

DFT calculations were performed using the generalized gradient approximation (GGA)[4] in the form of Perdew−Burke−Ernzerhof (PBE)[5] exchange−correlation functional with Vienna Ab initio Simulation Package (VASP).[6, 7] The empirical dispersion correction (D3)[8] in Grimme's scheme was employed to take into account of van der Waals (vdW) interaction. The projector augmented wave (PAW)[9] method was used to describe the core−valence electron interactions. The catalysts were a 1 × 1 × 1 supercell of surface of metal. The surface Brillouin zone was sampled with a 4 × 3 × 1 Monkhorst−Pack kpoint grid. The equilibrium geometries were obtained by minimizing the energy and the forces on the atoms to 10^{-5} eV and 0.03 eV/Å, respectively. The kinetic energy cutoff for the plane−wave basis set was set to be 500 eV. The vacuum space was set to be 15 Å in the z direction to avoid the interactions between two neighboring images.

The detailed reaction equations for the adsorption of NO_3^- and the desorption of NO_2^- are presented below:

$$* + NO_3^- \rightarrow *NO_3 + e^-$$

$$*NO_3 + 2H^+ + 2e^- \rightarrow *NO_2 + H_2O$$

$$*NO_2 + e^- \rightarrow * + NO_2^-$$

Where * represents the active site. Then, the reaction free energy change can be obtained by the following equation:

$$\Delta G = \Delta E + \Delta E_{ZPE} - T\Delta S + \Delta G_{pH} + eU$$

Where ΔE is the total energy difference before and after intermediate adsorbed, ΔE_{ZPE} is the zero−point energy, ΔS is the entropy change, T represents the finite temperature, e is the charge transferred, U is the applied potential, and ΔG_{pH} is considered as the correction free energy of H^+.[10]

To avoid directly computing the energy of charged NO_3^- and NO_2^-, gaseous HNO_3 and HNO_2 were used as a reference in the following steps:[11, 12]

$$HNO_3(g) \rightarrow HNO_3(l), \qquad \Delta G_1 = -0.075\ eV$$

$$HNO_3(l) \rightarrow H^+ + NO_3^-, \ \Delta G_2 = -0.317\ eV$$

$$* + NO_3^- \rightarrow *NO_3 + e^-$$

Hence, the adsorption energy of NO_3^- (ΔG_{*NO3}) can be approximately expressed as:

$$* + HNO_3(g) \rightarrow *NO_3 + 1/2\, H_2$$

$$\Delta G_{*NO3} = G_{*NO3} + 1/2\, G_{H2} - G_{HNO3(g)} - G_* + \Delta G_{correct}$$

$$\Delta G_{correct} = -\Delta G_1 - \Delta G_2$$

Where G_{*NO3}, G_*, $G_{HNO3(g)}$ and G_{H2} are the Gibbs free energy of NO_3^- adsorbed on active site, active site, HNO_3 and H_2 molecules in the gas phase, respectively. $\Delta G_{correct}$ denotes the correction of adsorption energy.[13] According to CRC handbook of chemistry and physics, $\Delta G_1 = -0.075$ eV and $\Delta G_2 = -0.317$ eV.

The correction free energy of H^+ (ΔG_{pH}) can be approximately expressed as:

$$\Delta G_{pH} = -k_B T \ln 10 * pH$$

Where k_B is the Boltzmann constant.

Similarly, the desorption energy of NO_2^- (ΔG_{NO2-}) can be approximately expressed as:

$$*NO_2 + 1/2\, H_2 \rightarrow * + HNO_2(g)$$

$$\Delta G_{NO2-} = G_{HNO2(g)} + G_* - G_{*NO2} - 1/2\, G_{H2} - \Delta G_{correct}$$

$$\Delta G_{correct} = -0.143\ eV$$

The Gibbs free energy of HER process could be calculated by

$$\Delta G_{HER} = G_* + 1/2\, G_{H2} - G_{*H}$$

1.11 The theoretical reduction potential of aqueous Zn−NO_3^- battery

The calculation process of theoretical reduction potential:

$$NO_3^- + 7H_2O + 8e^- \rightarrow NH_4OH + 9OH^- \text{，} pH = 14$$

$$E_{NO_3^-/NH_3} = -\frac{1}{nF}\left(\Delta G_{NO_3^-/NH_3} + RT\, ln \frac{[OH^-]^9\,[NH_4OH]}{[NO_3^-]}\right)$$

$$\Delta G_{NO_3^-/NH_3} = \Delta G_f^o(NH_4OH) + 9\Delta G_f^o(OH^-) - \Delta G_f^o(NO_3^-) - 7\Delta G_f^o(H_2O) = 119\ kJ\ mol^{-1}$$

Where $\Delta G_{NO_3^-/NH_3}$ is the standard molar Gibbs free energy change of the reaction at 298 K. Where Gibbs free energy of formation (ΔG_f^o) is indexed according Lange's Handbook of Chemistry. The $[OH^-]$, $[NH_4OH]$, and $[NO_3^-]$ in cathode are 1 mol L^{-1}, 1 mmol L^{-1}, and 0.1 mol L^{-1}, respectively. Where n, F, R, and T are the electron transfer number (8), the Faraday Constant (96485 C mol^{-1}), the gas constant (8.314 J mol^{-1} K^{-1}), and the reaction temperature (298 K), respectively. The calculation of theoretical reduction potential for other reactions is referred to above.

The electrochemical reactions of aqueous Zn−NO_3^- battery in the process of discharging are presented as following:

Cathode (1 M KOH with 0.1 M KNO_3, pH = 14):

$NO_3^- + 7H_2O + 8e^- \rightarrow NH_4OH + 9OH^-$ ， $E_{NO_3^-/NH_3} = -0.14\ V$

Cathode (1 M KOH with 1 M KNO_3, pH = 14):

$NO_3^- + 7H_2O + 8e^- \rightarrow NH_4OH + 9OH^-$ ， $E_{NO_3^-/NH_3} = -0.13\ V$

Anode (1 M KOH with 0.02 M $Zn(CH_3COO)_2$, pH = 14):

$4Zn + 8OH^- \rightarrow 4ZnO + 4H_2O + 8e^-$ ， $E_{ZnO/Zn} = -1.26\ V$

Overall reaction:

$4Zn + NO_3^- + 3H_2O \rightarrow 4ZnO + NH_4OH + OH^-$

$E_{discharging} = 1.12\ V$, $\left[NO_3^-\right] = 0.1\ M$

$E_{discharging} = 1.13\ V$, $\left[NO_3^-\right] = 1\ M$

The electrochemical reactions of aqueous Zn−NO_3^- battery in the process of charging are presented as following:

Cathode (1 M KOH with 0.1 M KNO_3, pH = 14):

$4OH^- \rightarrow O_2 + 2H_2O + 4e^-$ ， $E_{O_2/OH^-} = 0.40\ V$

Anode (1 M KOH with 0.02 M $Zn(CH_3COO)_2$, pH = 14):

$2ZnO + 2H_2O + 4e^- \rightarrow 2Zn + 4OH^-$ ， $E_{ZnO/Zn} = -1.26\ V$

Overall reaction:

$2ZnO \rightarrow 4Zn + O_2$,$E_{charging} = 1.66\ V$

1.12 The assembly of aqueous Zn−NO_3^- battery

The aqueous Zn−NO_3^- battery was executed in H−type cell, containing 40 mL cathode electrolyte (1 M KOH + KNO_3) and 40 mL anode electrolyte (1 M KOH + 0.02 M $(CH_3COO)_2Zn$). Specifically, the o−CoP/C@Cu_3P/CF and Zn plate, as the cathode and anode for the Zn−NO_3^- battery, were separated by Nafion 117 proton exchange membrane. The open circuit voltage and polarization curves were conducted using CHI 660E.

2. Supporting figures

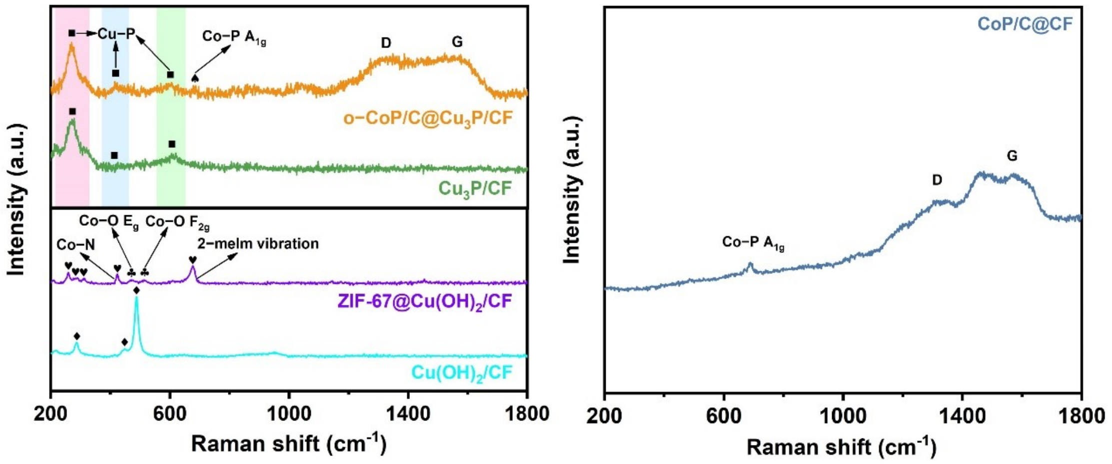

Fig. S1 a) Raman spectra of samples at different prepared period. b) Shell−isolated nanoparticle enhanced Raman spectra of CoP/C@CF.

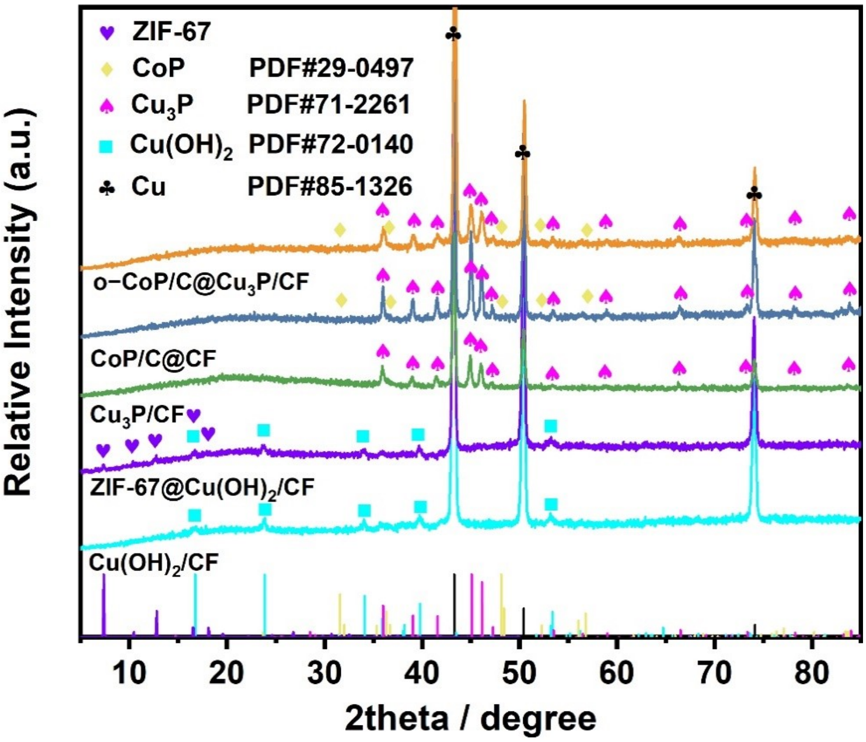

Fig. S2 XRD patterns of all precursors and contrast samples.

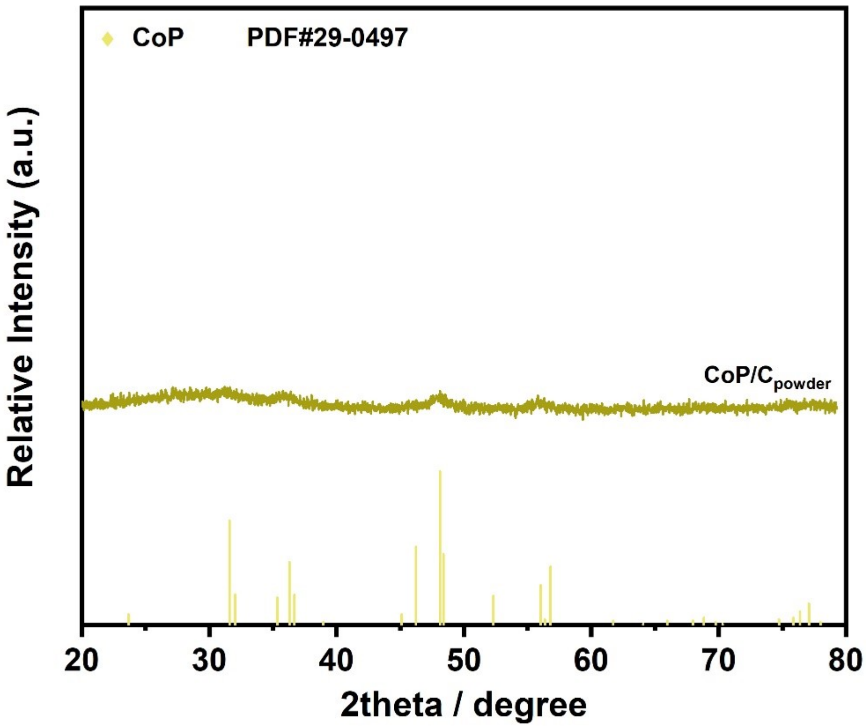

Fig. S3 XRD pattern of CoP/C$_{powder}$.

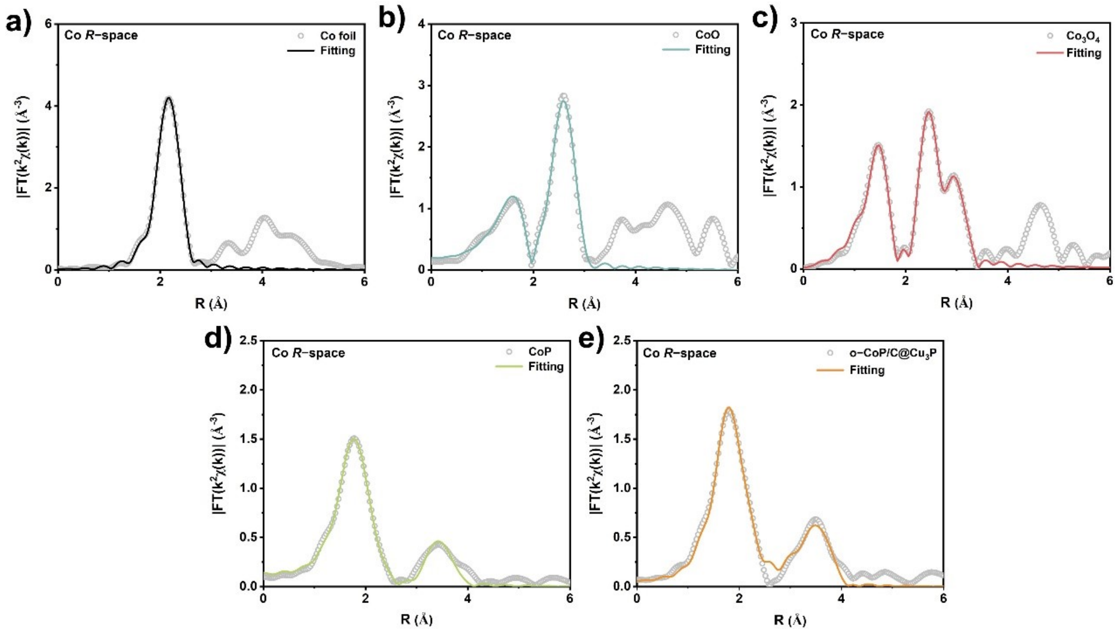

Fig. S4 The fitting Co K−edge FT−EXAFS spectra of a) Co foil, b) CoO, c) Co_3O_4, d) CoP and e) o−CoP/C@Cu_3P in R space.

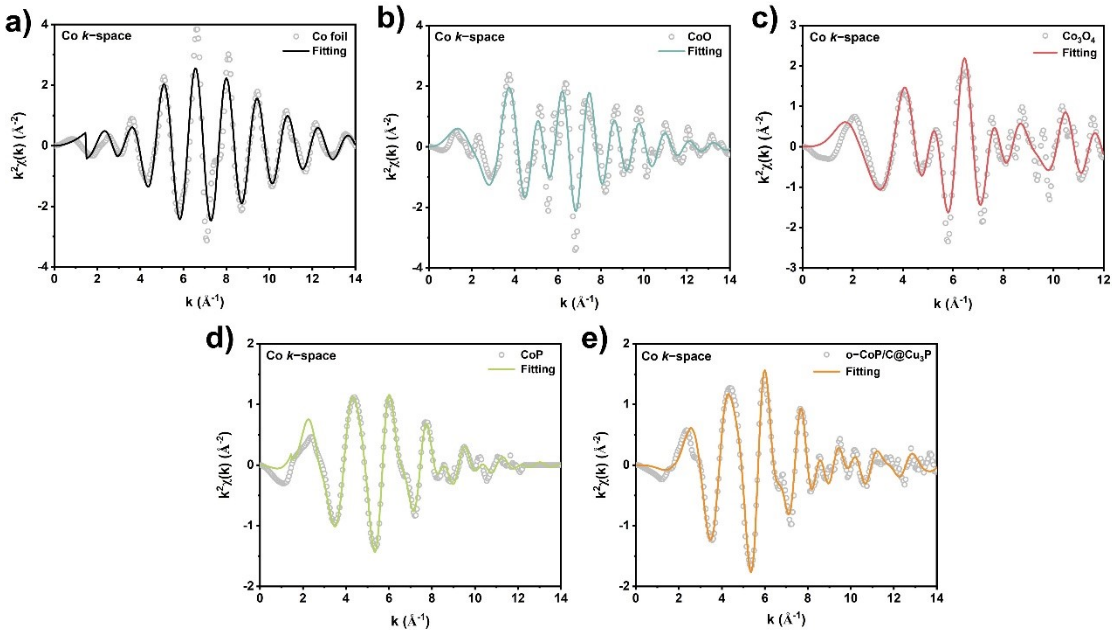

Fig. S5 The fitting Co K−edge FT−EXAFS spectra of a) Co foil, b) CoO, c) Co_3O_4, d) CoP and e) o−CoP/C@Cu_3P in k space.

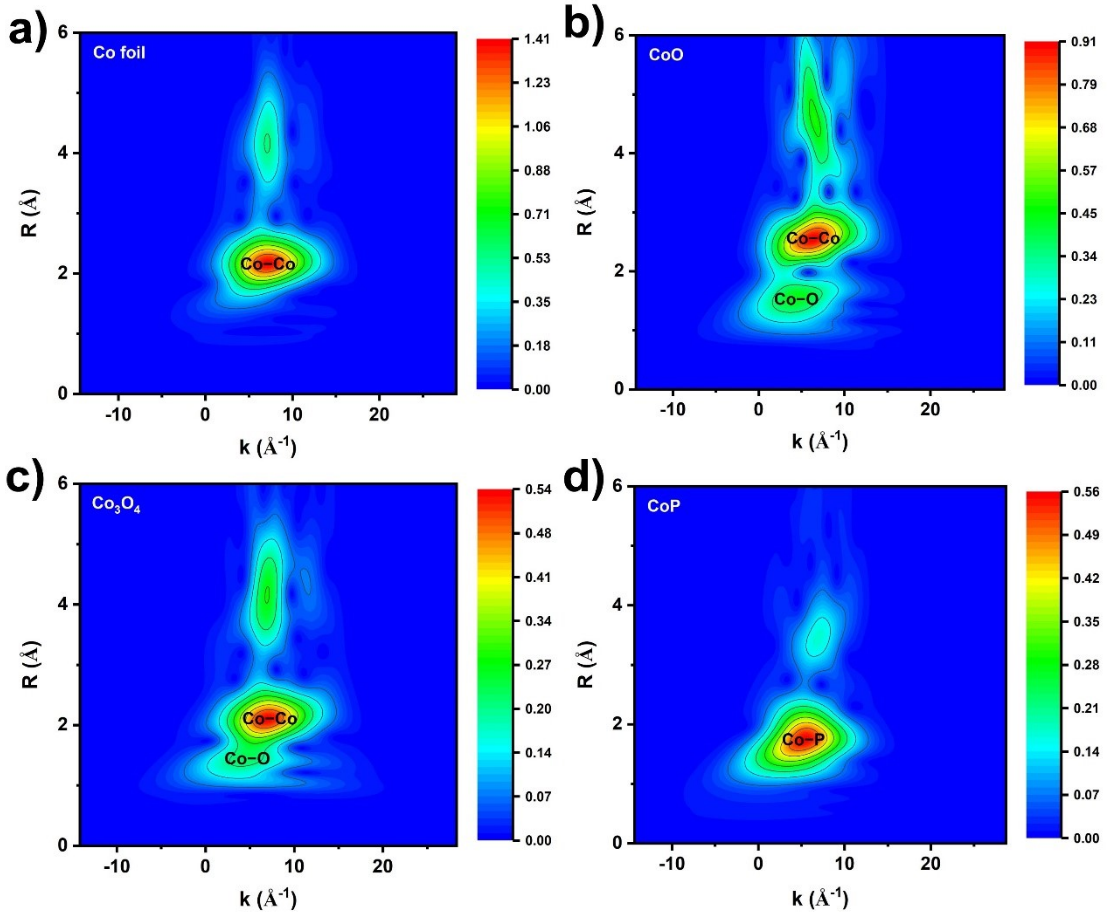

Fig. S6 The Co K−edge WT−EXAFS plots of a) Co foil, b) CoO, c) Co_3O_4, and d) CoP.

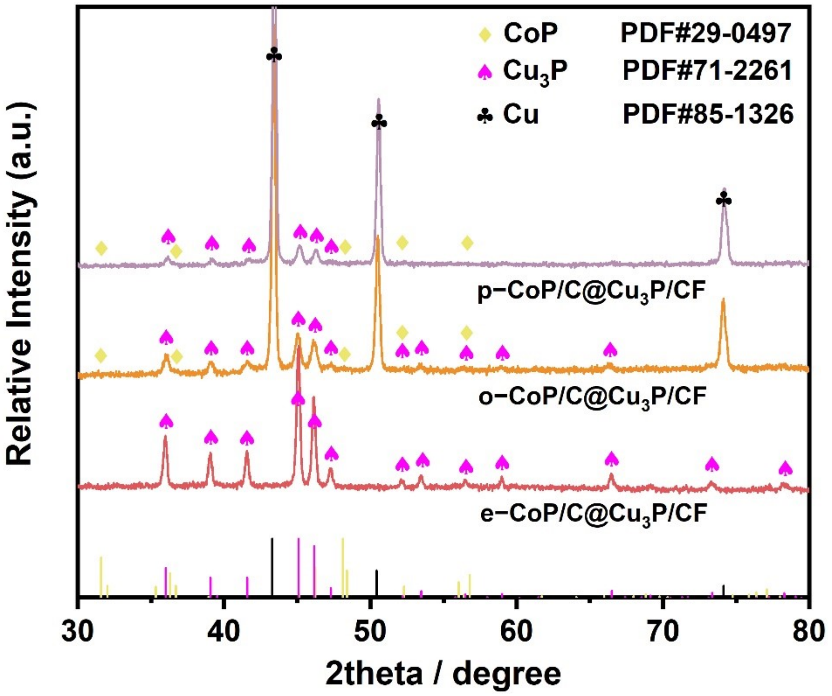

Fig. S7 XRD patterns of p−CoP/C@Cu_3P/CF, o−CoP/C@Cu_3P/CF, and e−CoP/C@Cu_3P/CF.

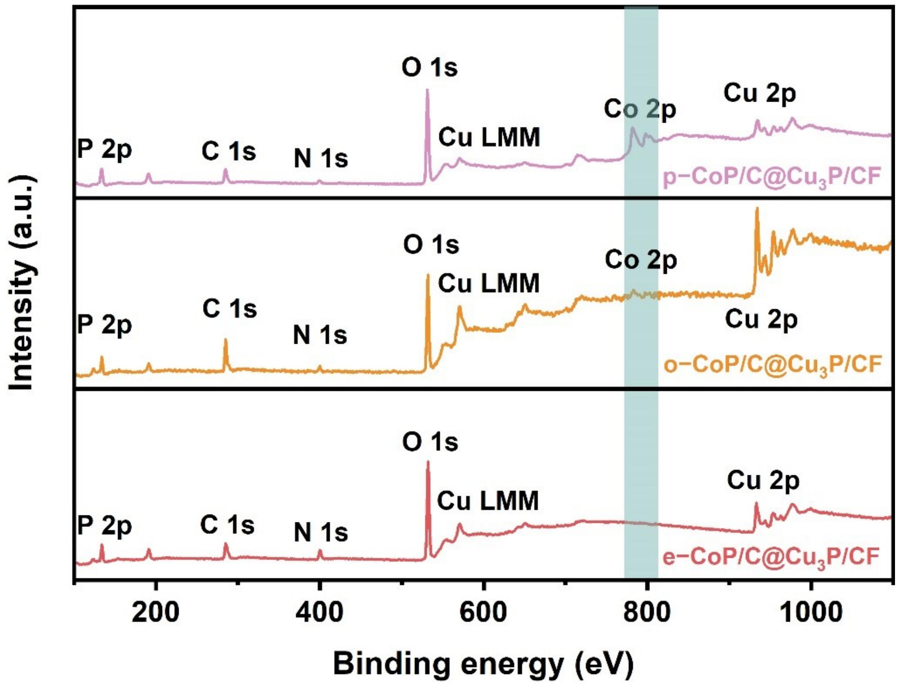

Fig. S8 XPS survey spectra of p−CoP/C@Cu_3P/CF, o−CoP/C@Cu_3P/CF, and e−CoP/C@Cu_3P/CF.

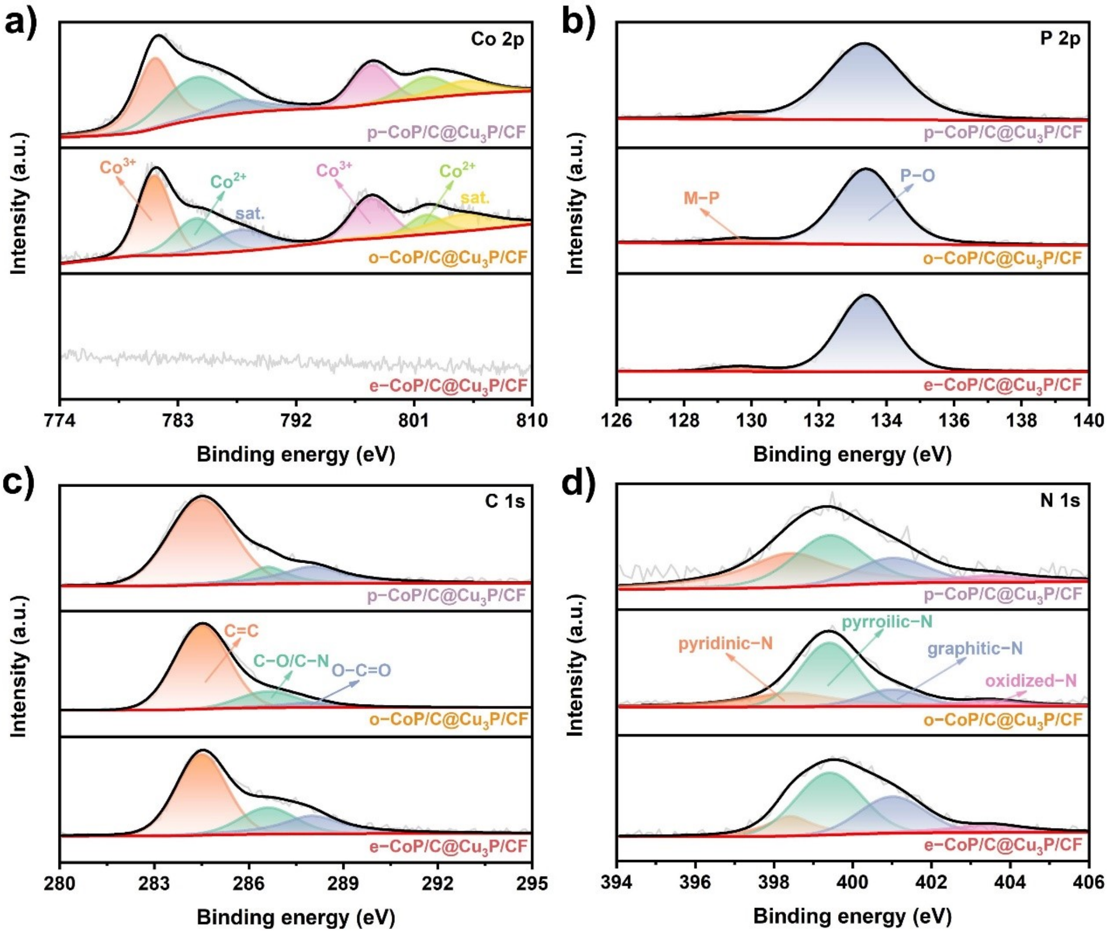

Fig. S9 a) Co 2p, b) P 2p, c) C 1s, and d) N 1s spectra of CoP/C@Cu_3P/CF with different phosphorus−modulation.

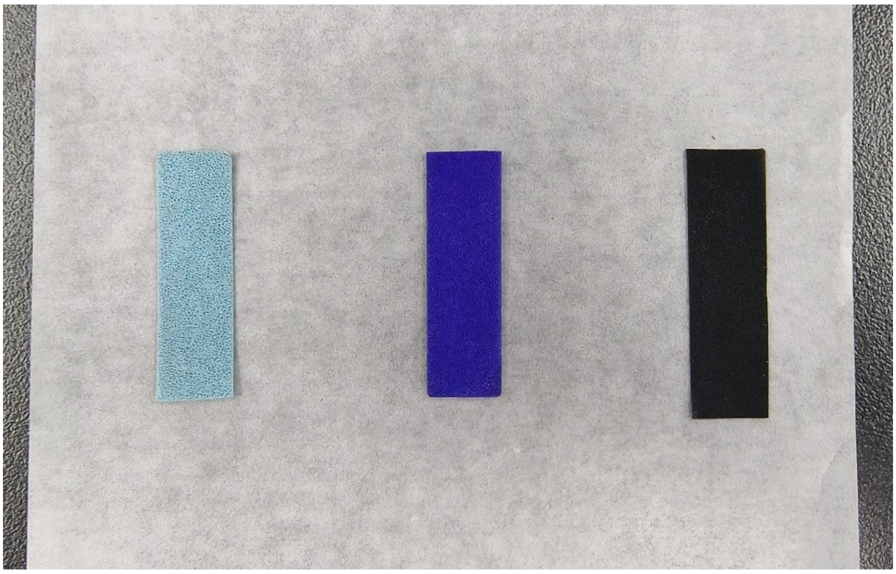

Fig. S10 Photograph of $Cu(OH)_2$/CF (left), ZIF−67@ $Cu(OH)_2$/CF (mid), and o−CoP/C@Cu_3P/CF (right).

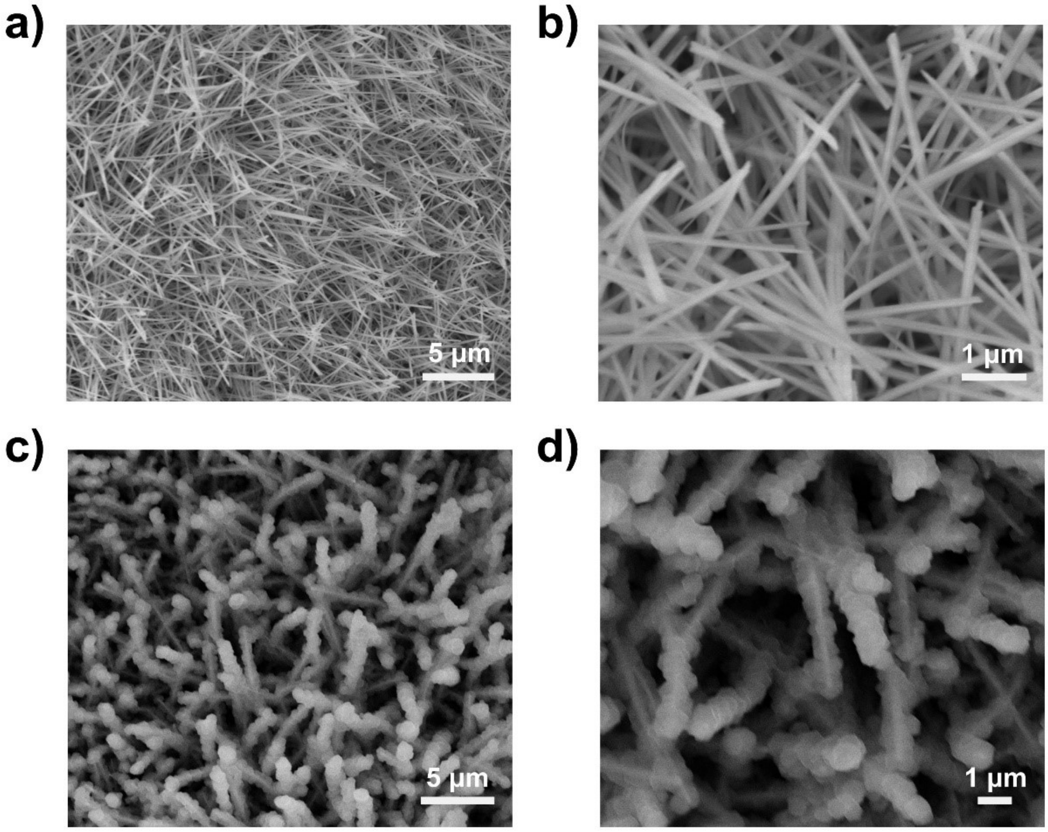

Fig. S11 SEM images of $Cu(OH)_2$/CF and ZIF−67@$Cu(OH)_2$/CF.

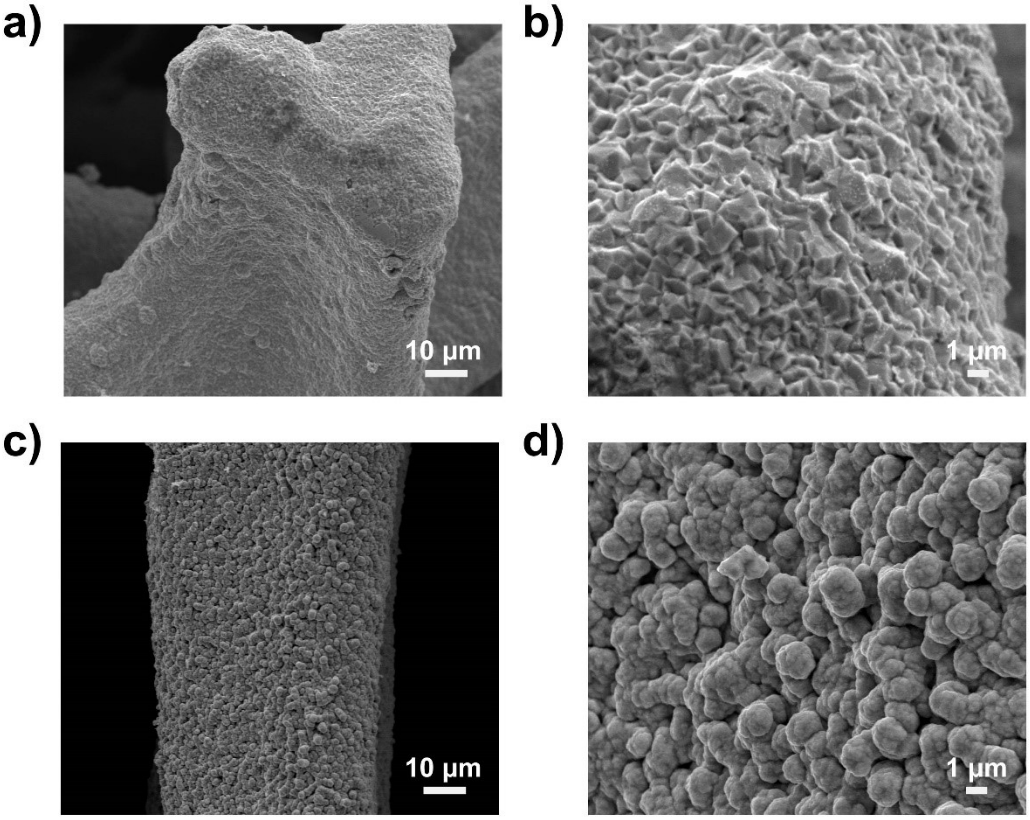

Fig. S12 SEM images of CoP/C@CF and Cu_3P/CF.

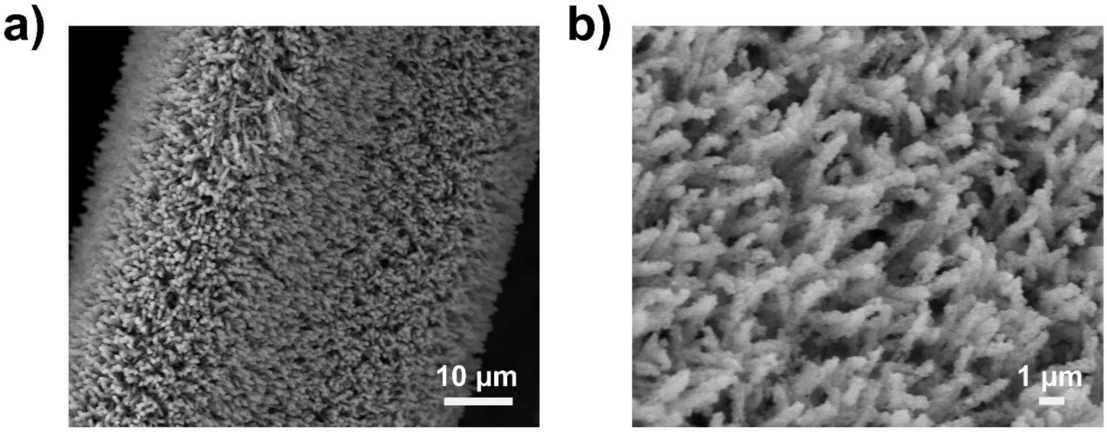

Fig. S13 SEM images of p−CoP/C@Cu_3P/CF.

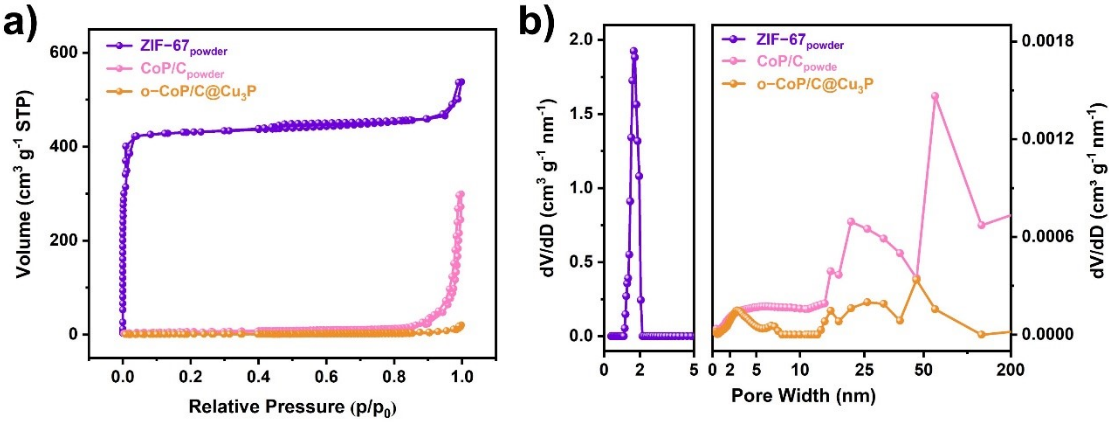

Fig. S14 Nitrogen adsorption−desorption isotherms and the corresponding pore size distributions of ZIF−67$_{powder}$, CoP$_{powder}$, and o−CoP/C@Cu_3P.

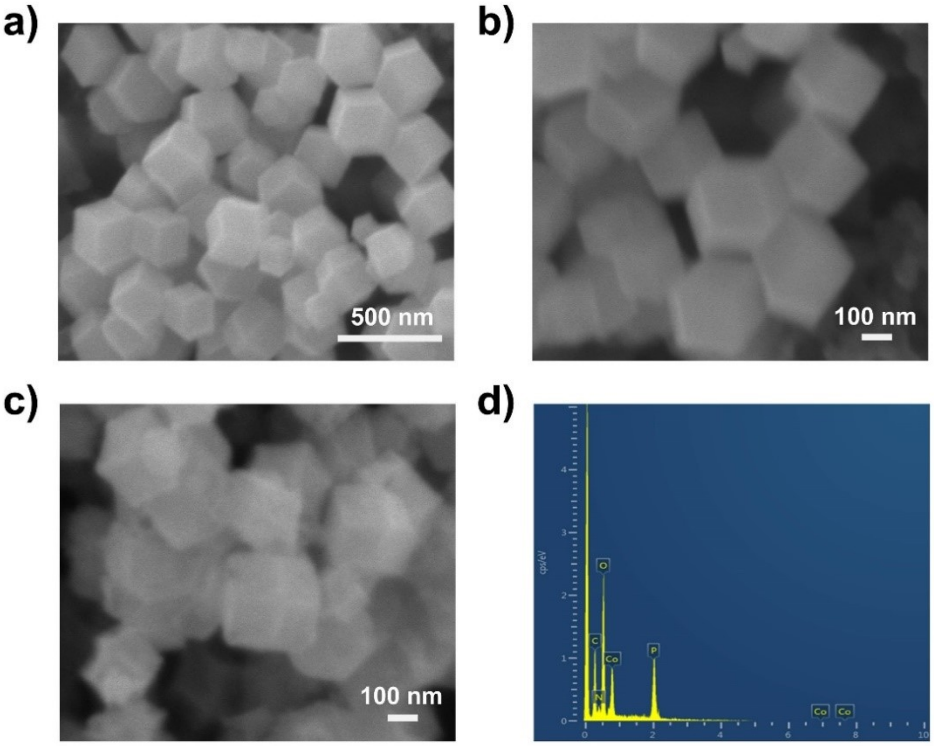

Fig. S15 SEM images of ZIF−67_{powder}, CoP_{powder}, and corresponding EDS analysis.

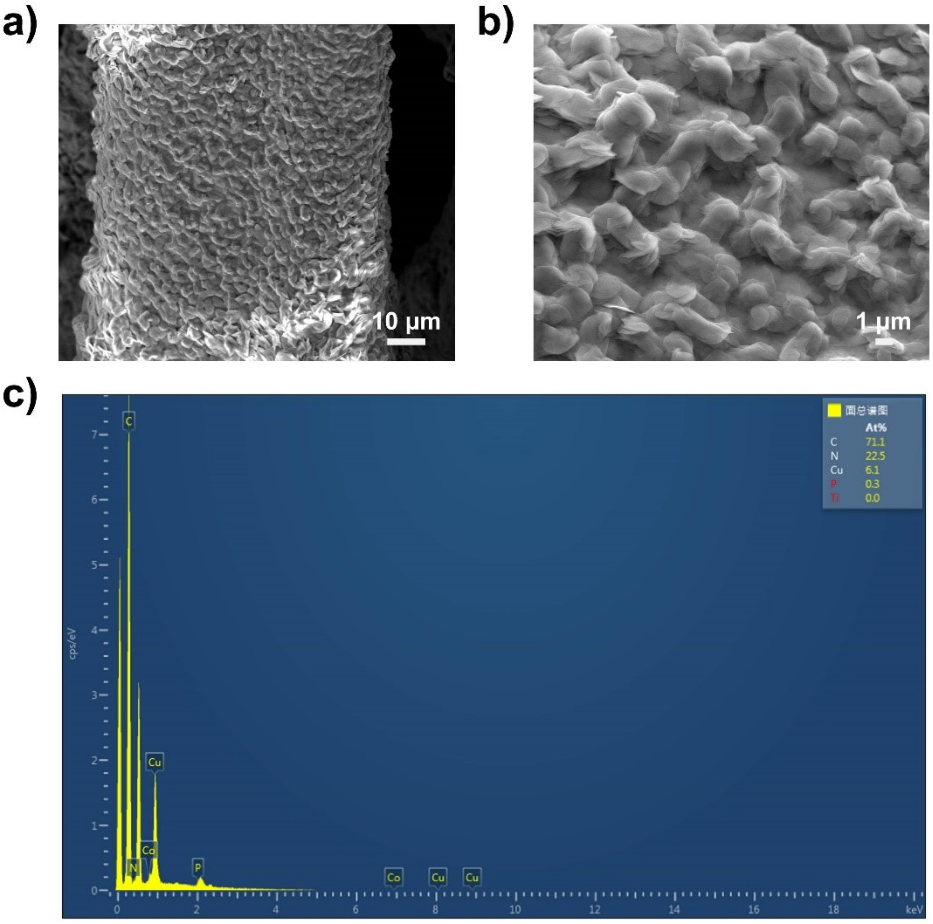

Fig. S16 SEM images of e−CoP/C@Cu_3P/CF and corresponding EDS analysis.

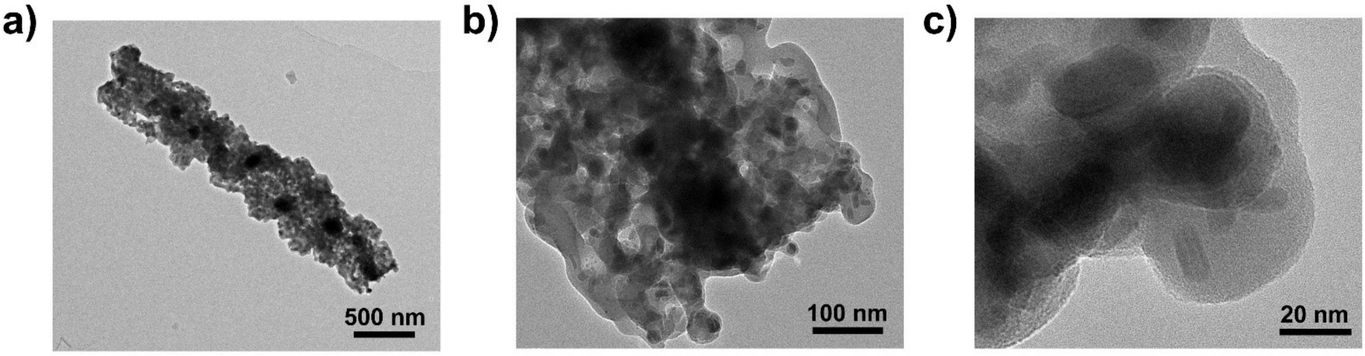

Fig. S17 STEM images of o−CoP/C@Cu$_3$P/CF.

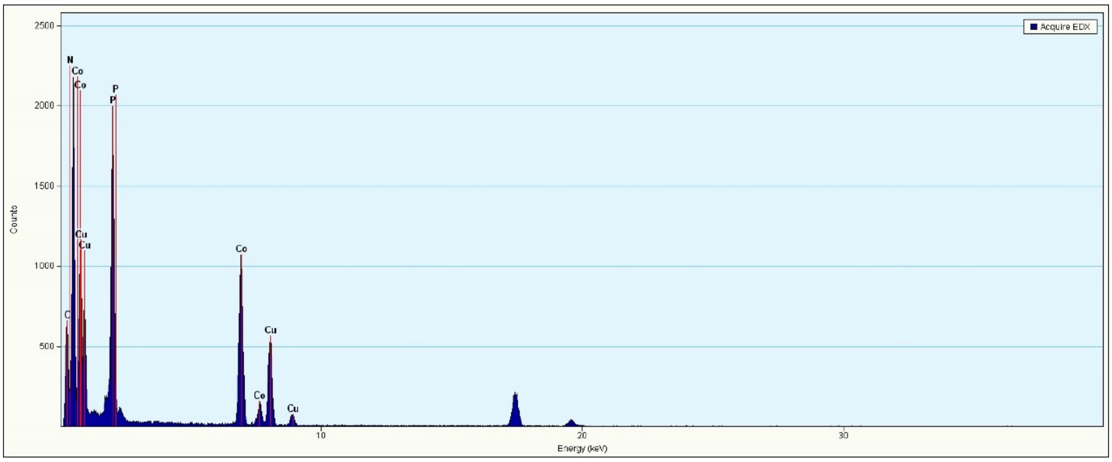

Fig. S18 EDS analysis of o−CoP/C@Cu$_3$P/CF.

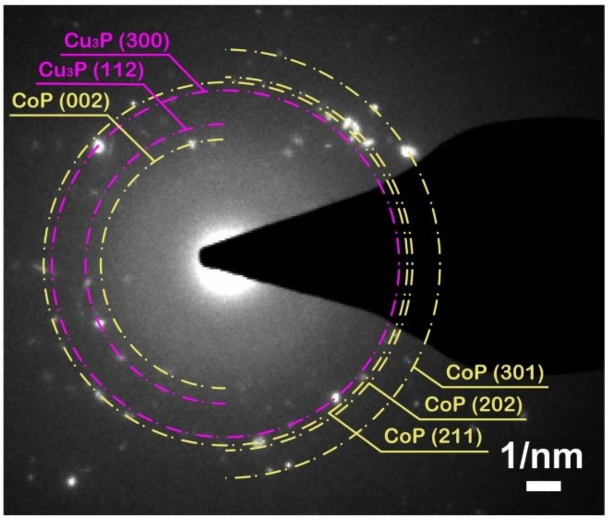

Fig. S19 The SAED pattern of o−CoP/C@Cu$_3$P/CF.

Fig. S20 Schematic illustration of H−type cell.

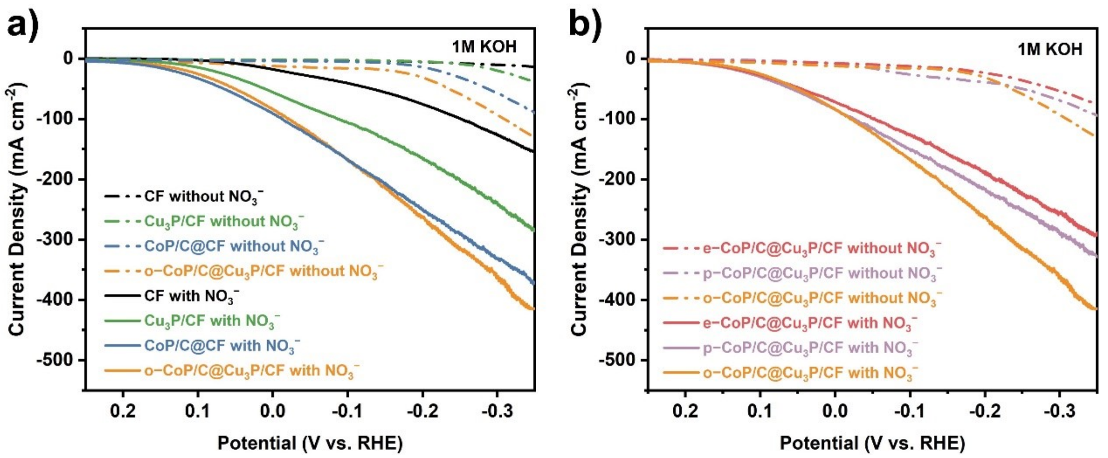

Fig. S21 a) LSV curves of CF, Cu_3P/CF, CoP/C@CF, and o−CoP/C@ Cu_3P/CF in 1 M KOH with and without 0.1 M KNO_3. b) LSV curves of CoP/C@Cu_3P/CF based on different phosphating degree in 1 M KOH with and without 0.1 M KNO_3.

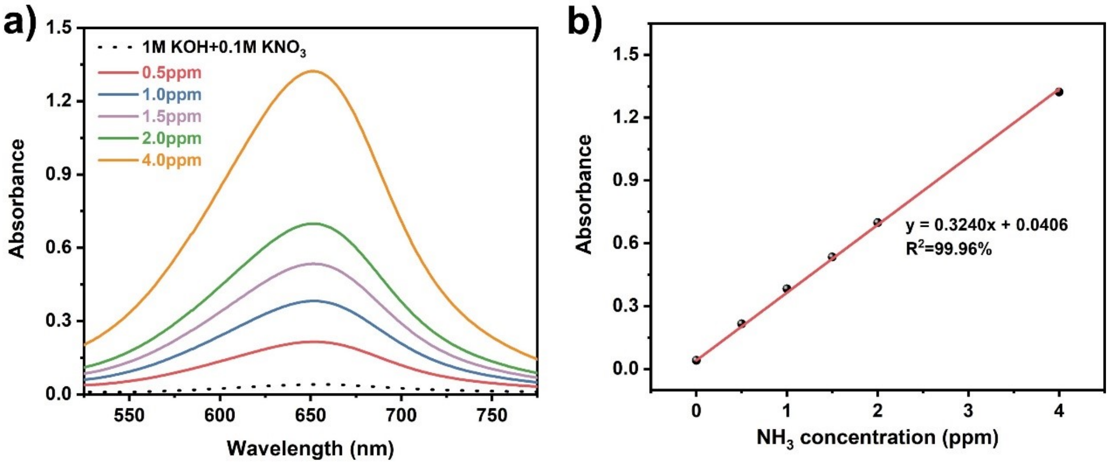

Fig. S22 The electrolyte stained with indophenol reagent using NH_4Cl solutions with specific concentration as standards. a) UV−vis spectrums, and b) calibration curves used for determining NH_3 concentration. The absorbance at 655 nm was measured by a UV−vis spectrophotometer, and the fitting curve shows good linear correlation of absorbance with NH_3 concentration.

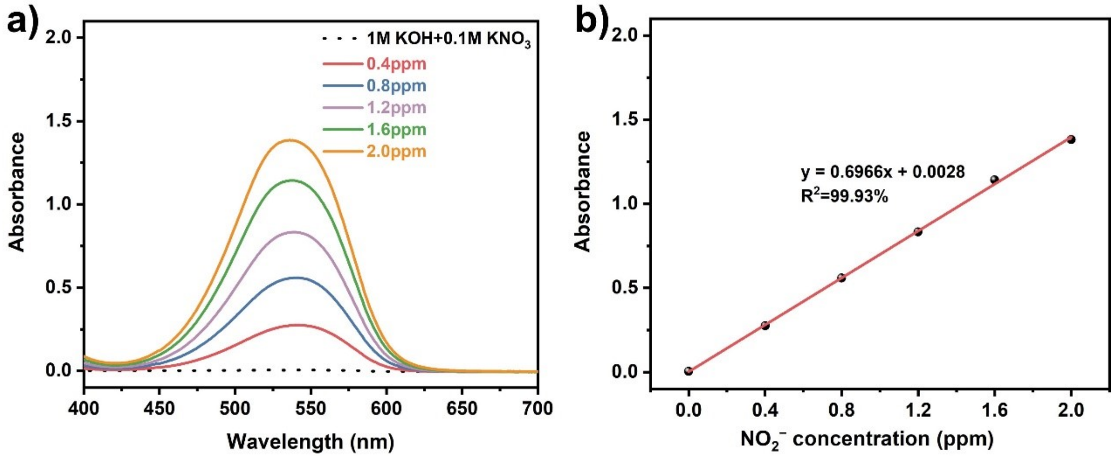

Fig. S23 The electrolyte stained with Griess reagent using NO_2^- solutions with specific concentration as standards. a) UV−vis spectrums, and b) calibration curves used for determining NO_2^- concentration. The absorbance at 540 nm was measured by a UV−vis spectrophotometer, and the fitting curve shows good linear correlation of absorbance with NO_2^- concentration.

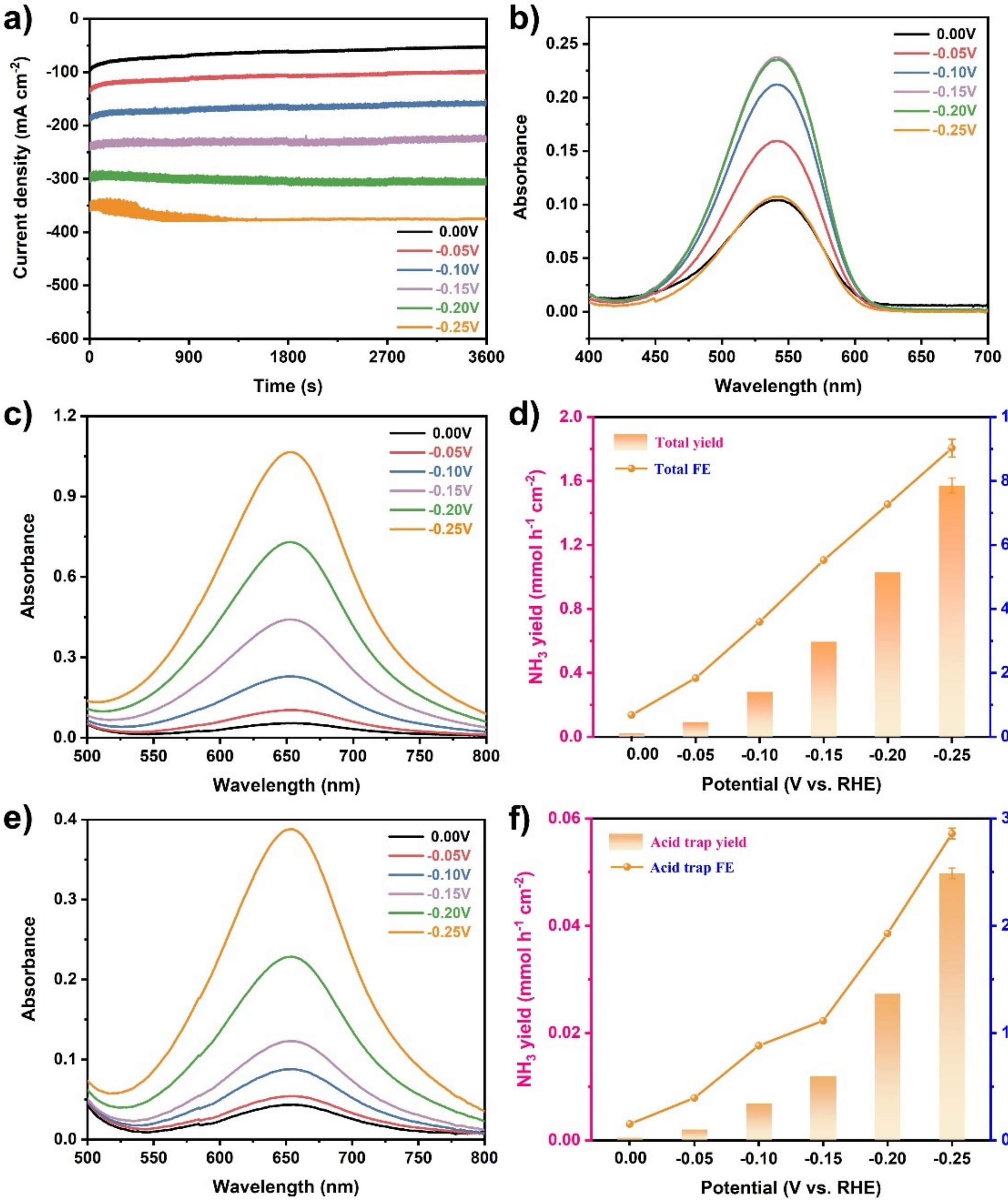

Fig. S24 The NITRR performance of o−CoP/C@Cu$_3$P/CF. a) CA curves, and b) UV−vis spectrums of the electrolyte (stained with Griess reagent) after 1 h electrocatalysis for o−CoP/C@Cu$_3$P/CF at different potentials. c) UV−vis spectrums, and d) total NH$_3$ yield and FE$_{NH3}$ of the electrolyte in H−type cell and acid trap (stained with indophenol reagent) after 1 h electrocatalysis for o−CoP/C@Cu$_3$P/CF at different potentials. e) UV−vis spectrums, and f) NH$_3$ yield and FE$_{NH3}$ of the electrolyte in acid trap (stained with indophenol reagent) after 1 h electrocatalysis for o−CoP/C@Cu$_3$P/CF at different potentials.

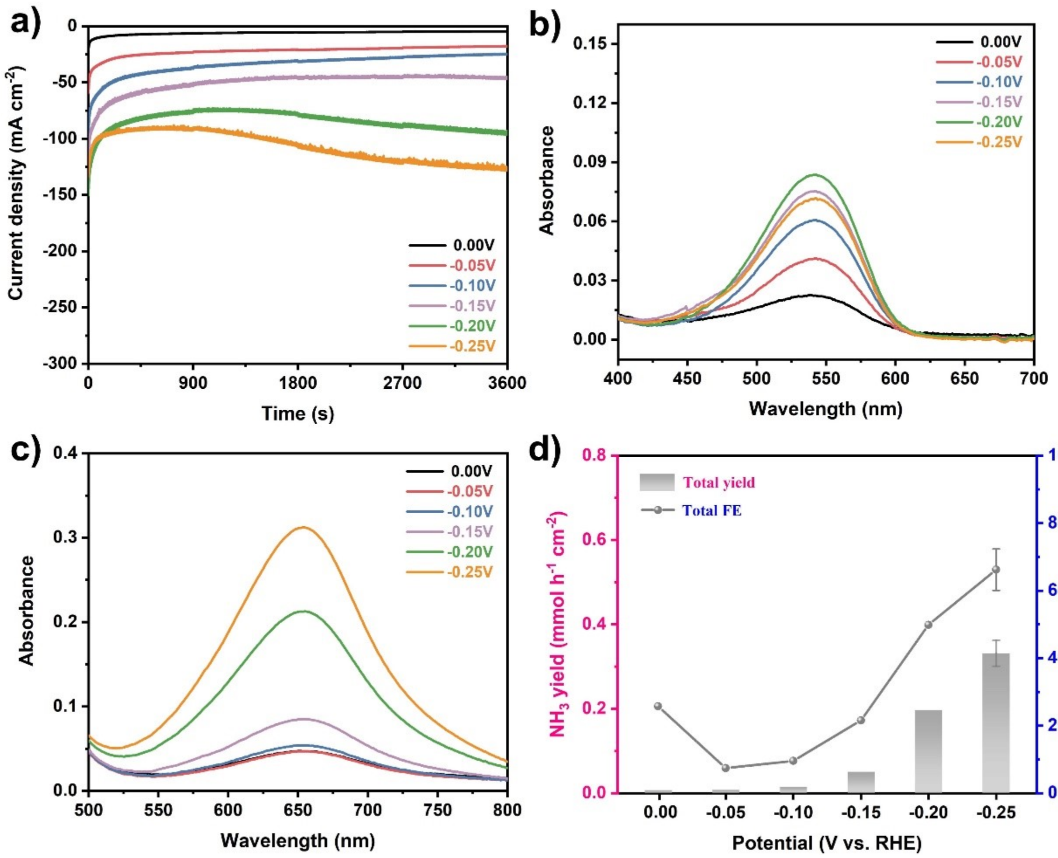

Fig. S25 The NITRR performance of CF. a) CA curves, and b) UV−vis spectrums of the electrolyte (stained with Griess reagent) after 1 h electrocatalysis for CF at different potentials. c) UV−vis spectrums, and d) total NH_3 yield and FE_{NH3} of the electrolyte in H−type cell and acid trap (stained with indophenol reagent) after 1 h electrocatalysis for CF at different potentials.

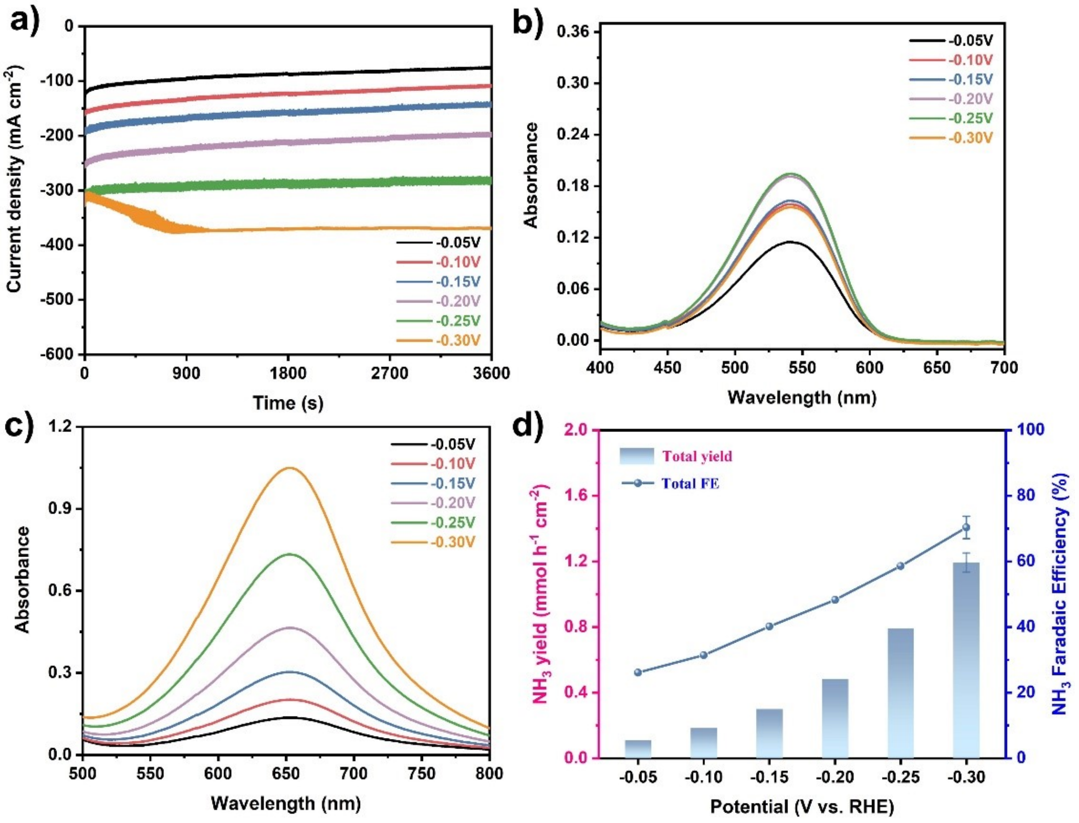

Fig. S26 The NITRR performance of CoP/C@CF. a) CA curves, and b) UV−vis spectrums of the electrolyte (stained with Griess reagent) after 1 h electrocatalysis for CoP/C@CF at different potentials. c) UV−vis spectrums, and d) total NH$_3$ yield and FE$_{NH3}$ of the electrolyte in H−type cell and acid trap (stained with indophenol reagent) after 1 h electrocatalysis for CoP/C@CF at different potentials.

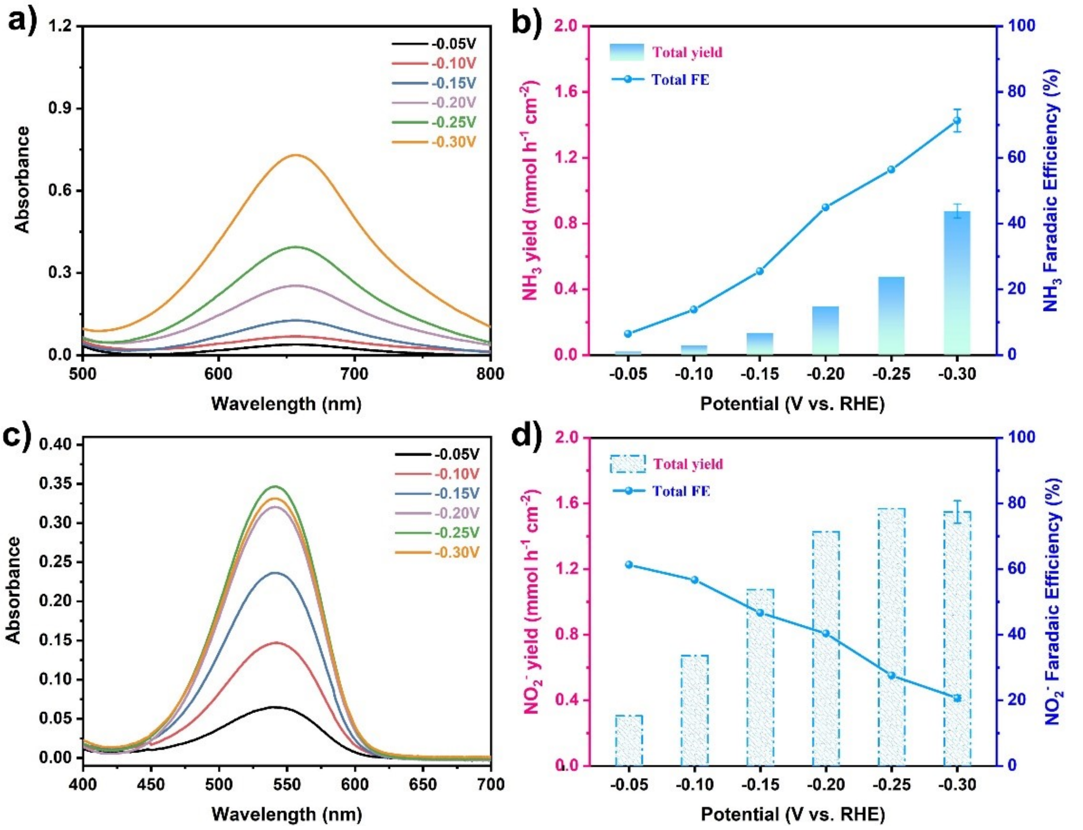

Fig. S27 The NITRR performance of CoP/C$_{powder}$@CF. a) UV−vis spectrums, b) total NH$_3$ yield and FE$_{NH3}$ of the electrolyte in H−type cell and acid trap (stained with indophenol reagent) after 1 h electrocatalysis for CoP/C$_{powder}$@CF at different potentials. c) UV−vis spectrums, d) total NO$_2^-$ yield and FE$_{NO2-}$ of the electrolyte in H−type cell and acid trap (stained with Griess reagent) after 1 h electrocatalysis for CoP/C$_{powder}$@CF at different potentials.

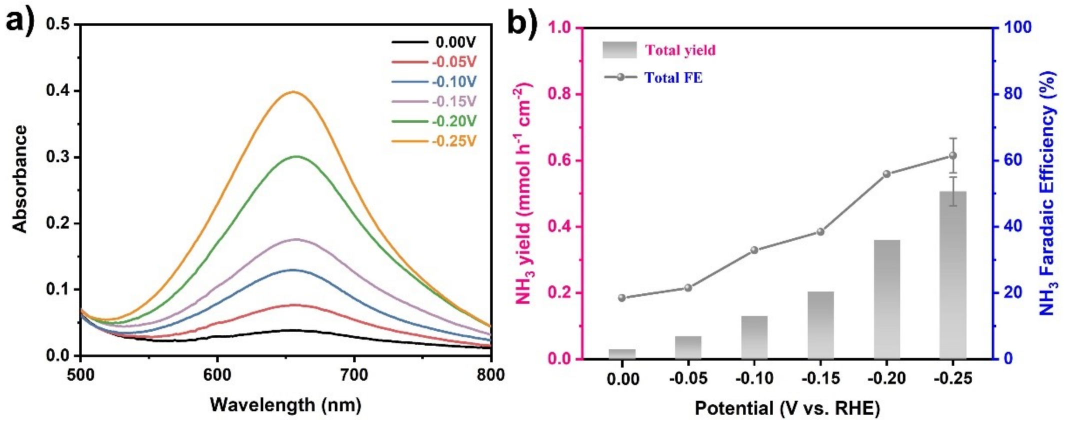

Fig. S28 The NITRR performance of CN$_{powder}$@CF. a) UV−vis spectrums, and b) total NH$_3$ yield and FE$_{NH3}$ of the electrolyte in H−type cell and acid trap (stained with indophenol reagent) after 1 h electrocatalysis for CN$_{powder}$@CF at different potentials.

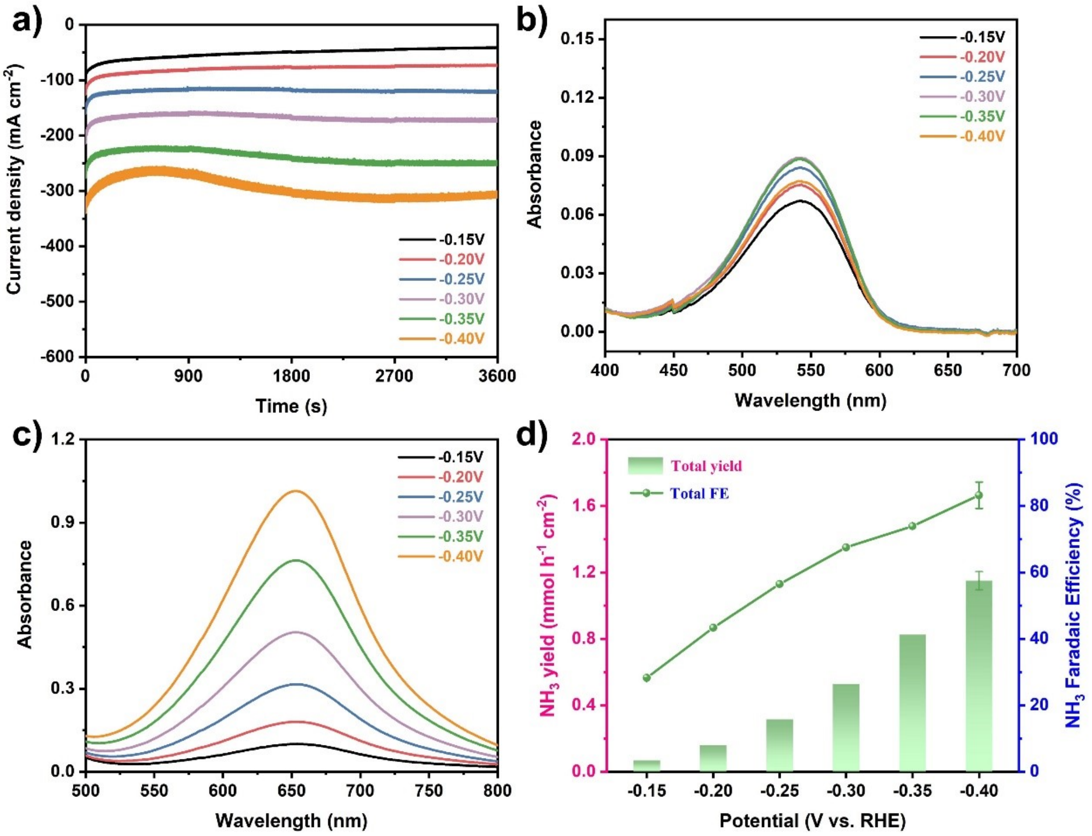

Fig. S29 The NITRR performance of Cu_3P/CF. a) CA curves, and b) UV−vis spectrums of the electrolyte (stained with Griess reagent) after 1 h electrocatalysis for Cu_3P/CF at different potentials. c) UV−vis spectrums, and d) total NH_3 yield and FE_{NH3} of the electrolyte in H−type cell and acid trap (stained with indophenol reagent) after 1 h electrocatalysis for Cu_3P/CF at different potentials.

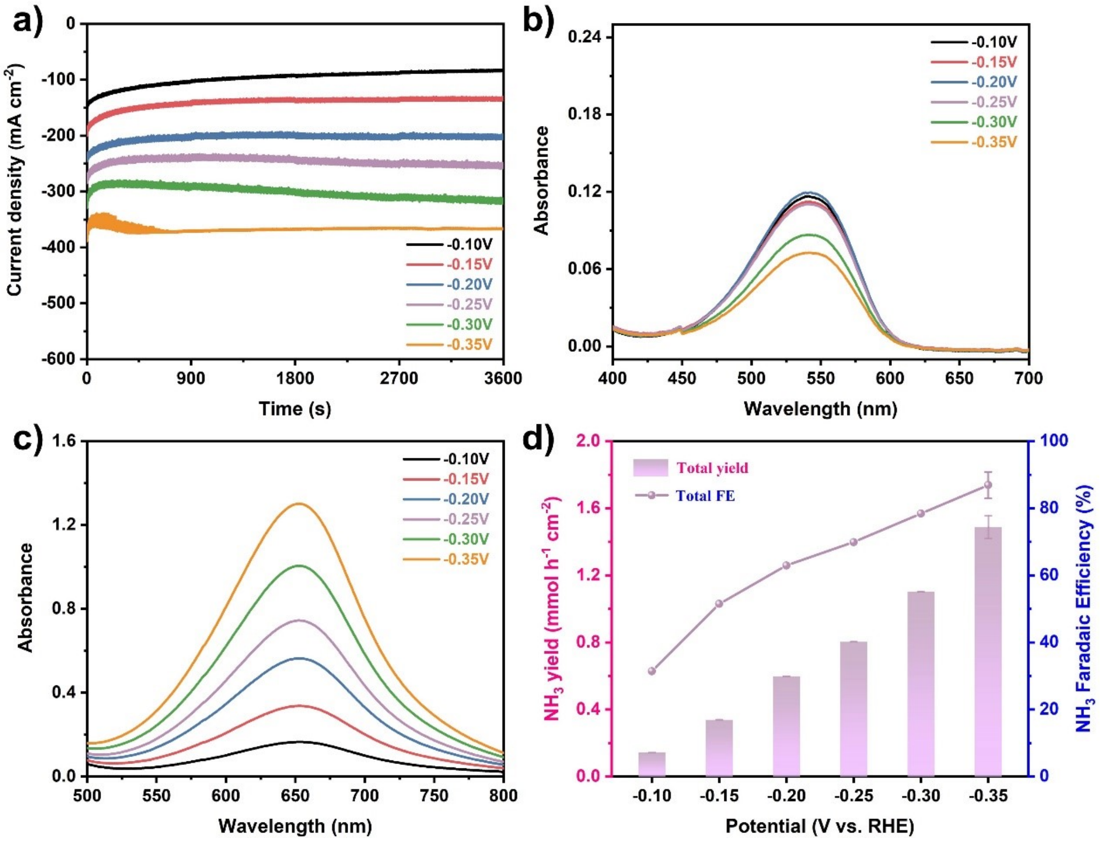

Fig. S30 The NITRR performance of p−CoP/C@Cu_3P/CF. a) CA curves, and b) UV−vis spectrums of the electrolyte (stained with Griess reagent) after 1 h electrocatalysis for p−CoP/C@Cu_3P/CF at different potentials. c) UV−vis spectrums, and d) total NH_3 yield and FE_{NH3} of the electrolyte in H−type cell and acid trap (stained with indophenol reagent) after 1 h electrocatalysis for p−CoP/C@Cu_3P/CF at different potentials.

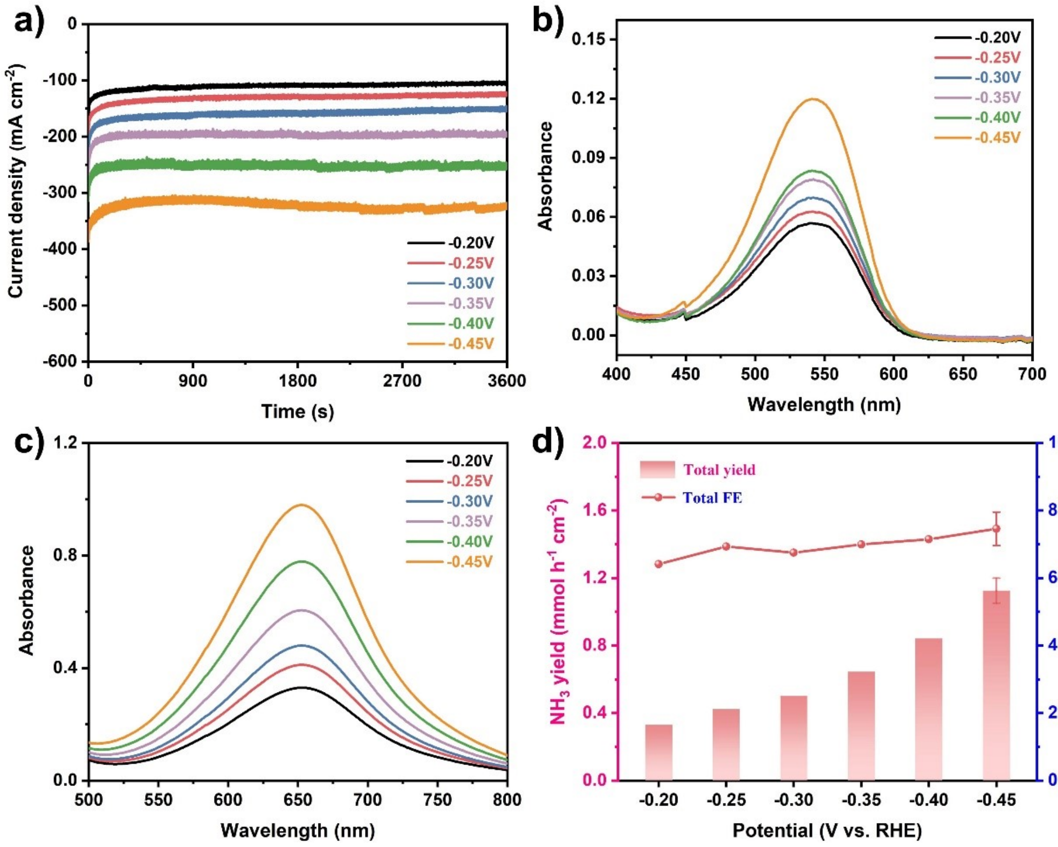

Fig. S31 The NITRR performance of e−CoP/C@Cu$_3$P/CF. a) CA curves, and b) UV−vis spectrums of the electrolyte (stained with Griess reagent) after 1 h electrocatalysis for e−CoP/C@Cu$_3$P/CF at different potentials. c) UV−vis spectrums, and d) total NH$_3$ yield and FE$_{NH3}$ of the electrolyte in H−type cell and acid trap (stained with indophenol reagent) after 1 h electrocatalysis for e−CoP/C@Cu$_3$P/CF at different potentials.

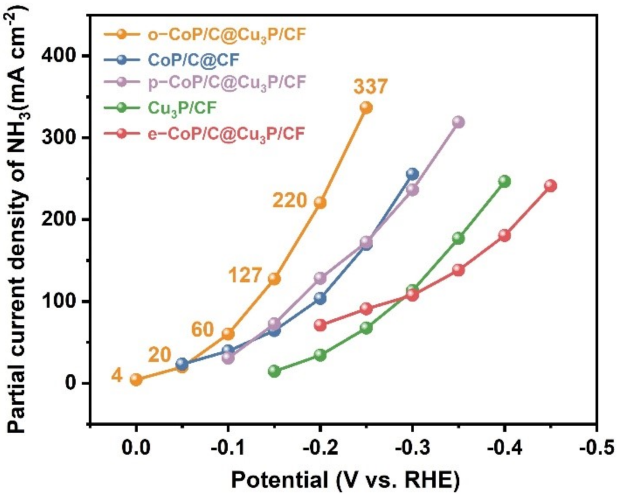

Fig. S32 The partial current density of NH_3 for all samples at different potential.

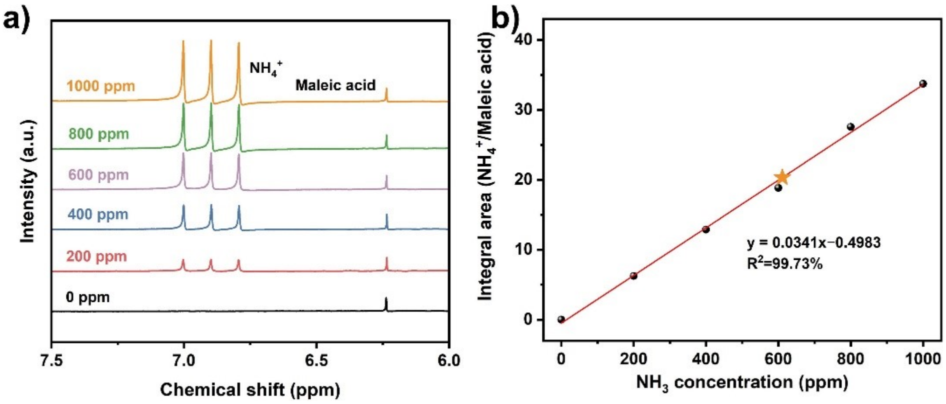

Fig. S33 The ^{1}H NMR spectra and calibration curves of electrolyte containing specific concentration NH_4Cl as standards.

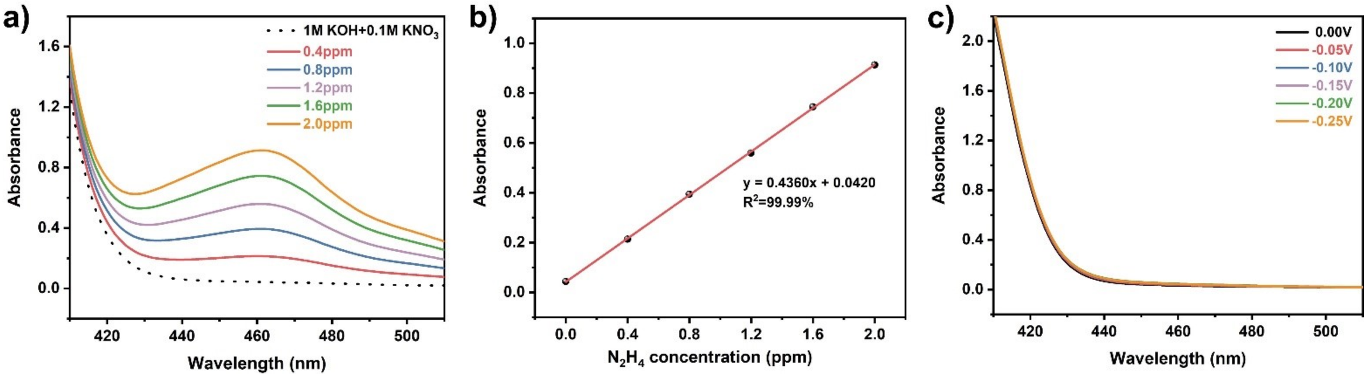

Fig. S34 The electrolyte stained with dimethylaminobenzaldehyde reagent using N_2H_4 solutions with specific concentration as standards. a) UV−vis spectrums, and b) calibration curves used for estimation of N_2H_4 concentration. c) UV−vis spectrums of the electrolyte (stained with dimethylaminobenzaldehyde reagent) after 1 h electrocatalysis for o−CoP/C@Cu$_3$P/CF at different potentials. The absorbance at 460 nm was measured by a UV−vis spectrophotometer, and the fitting curve shows good linear correlation of absorbance with N_2H_4 concentration.

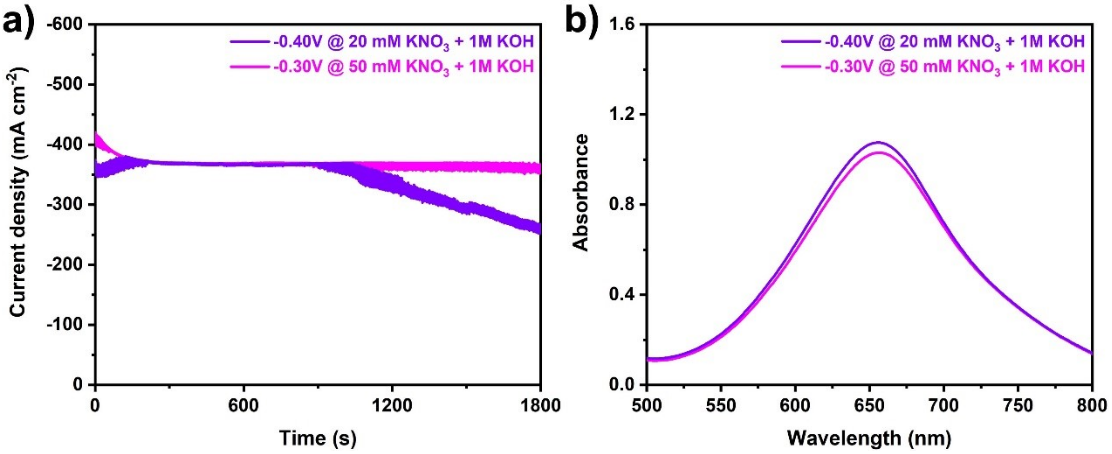

Fig. S35 The NITRR performance of o−CoP/C@Cu_3P/CF at different potentials in 1 M KOH electrolyte with various concentrations of NO_3^-. a) CA curves, and b) UV−vis spectrums of the electrolyte (stained with indophenol reagent) after 30 min electrocatalysis for o−CoP/C@Cu_3P/CF at various concentrations of NO_3^-.

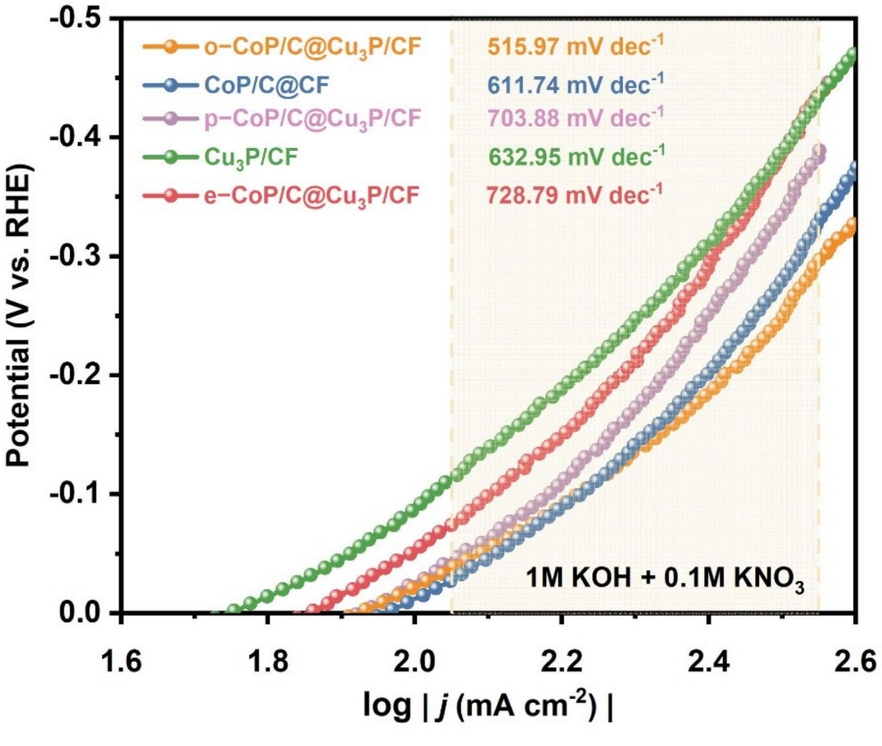

Fig. S36 Tafel slopes of all samples in Ar−saturated 1 M KOH electrolyte with 0.1 M KNO_3.

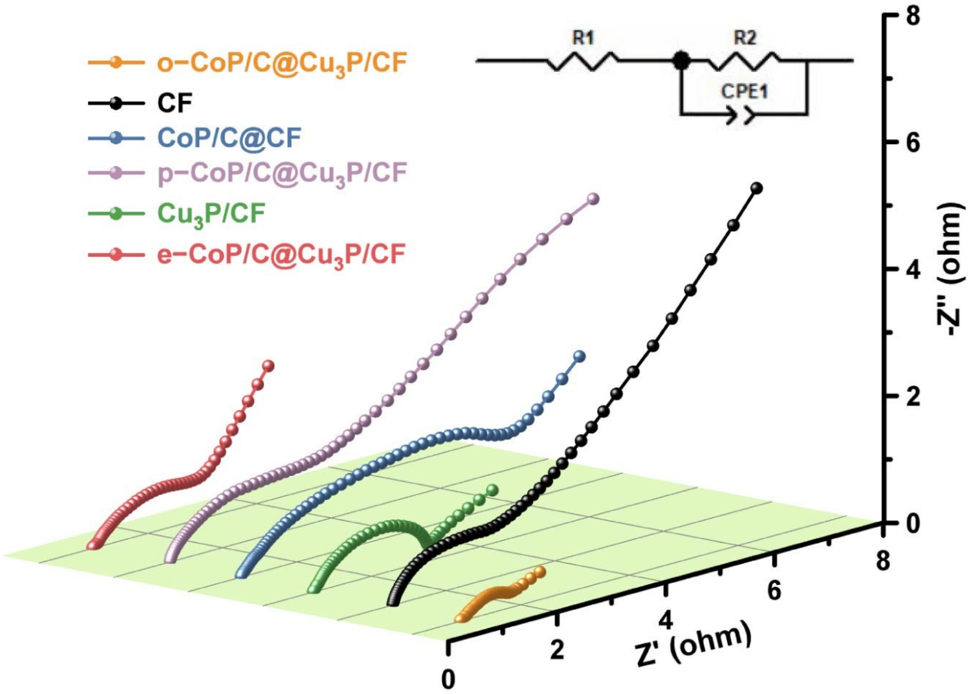

Fig. S37 Nyquist plots of all samples in Ar−saturated 1 M KOH electrolyte with 0.1 M KNO_3.

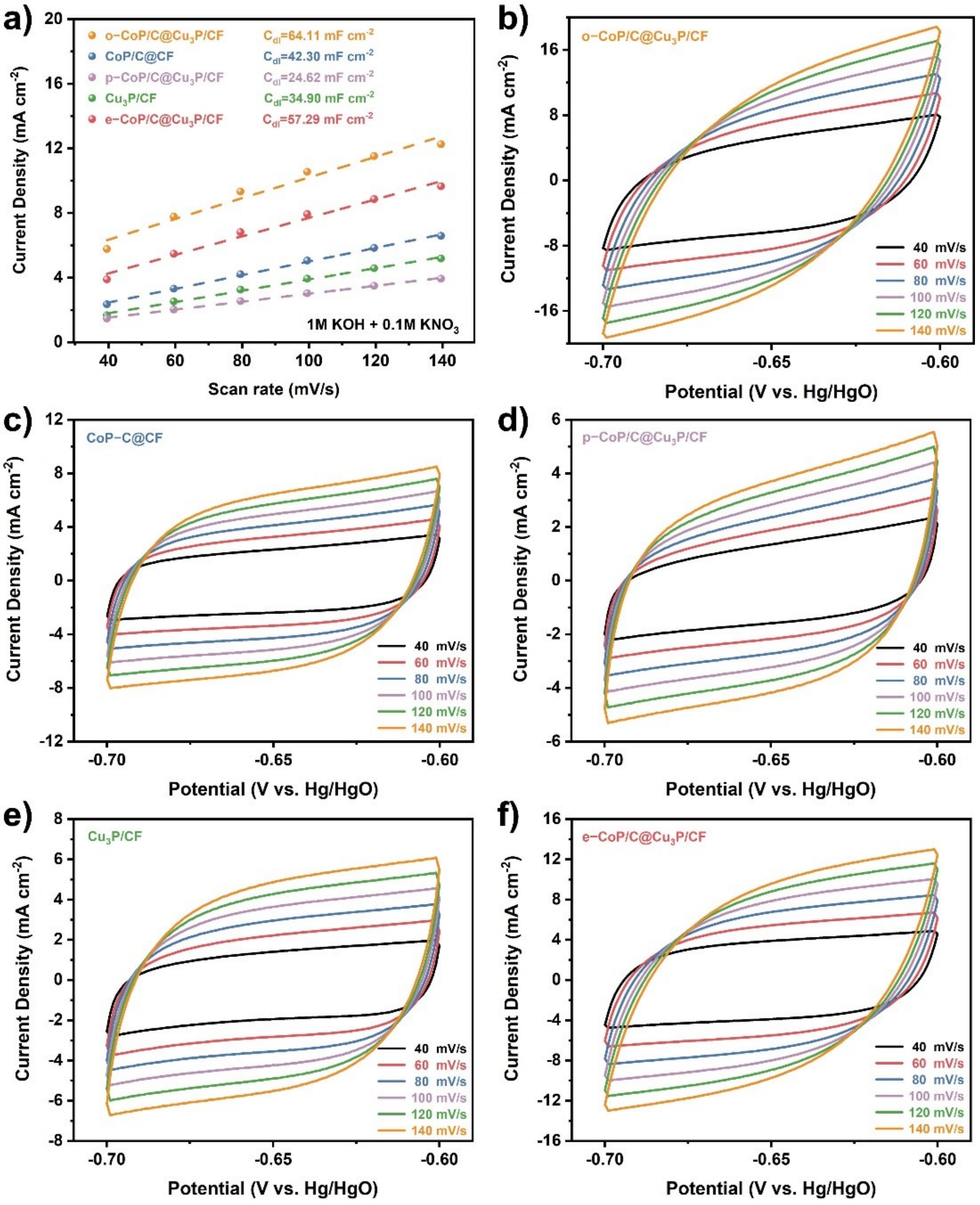

Fig. S38 C_{dl} and capacitance curves of all samples. a) The capacitive current density difference ($\Delta J = (J_+ - J_-)/2$) at −0.65 V vs. Hg/HgO as a function of scan rates for all samples. CV curves of b) o−CoP/C@Cu_3P/CF, c) Cu_3P/CF, d) CoP/C@ CF, e) p−CoP/C@Cu_3P/CF, and (f) o−CoP/C@Cu_3P/CF samples at various scan rates (40 to 140 mV s^{-1}) in the region of −0.60 to −0.70 V *vs. Hg/HgO*.

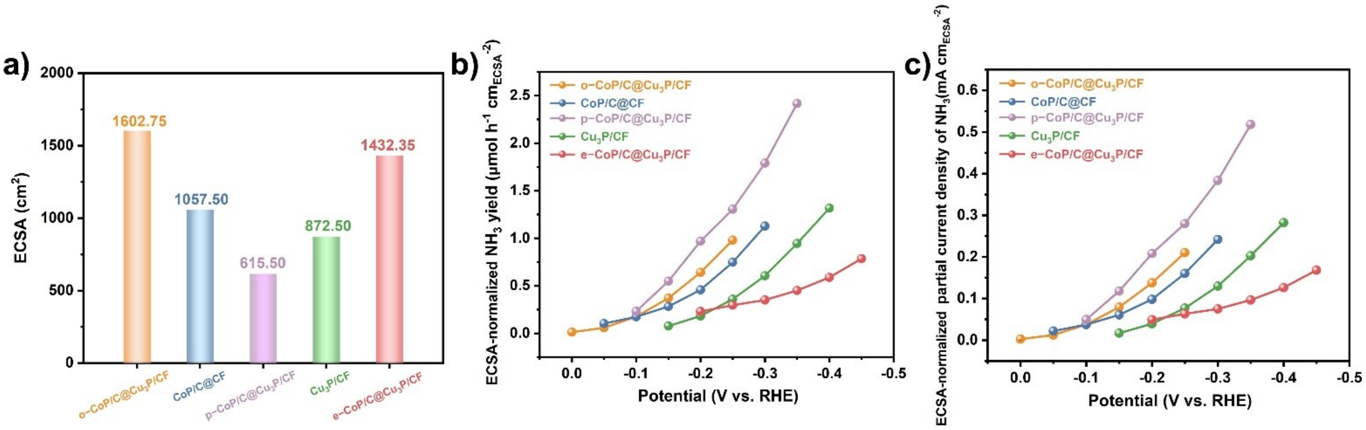

Fig. S39 The determination of ECSA. a) ECSAs of all samples. b) ECSA−normalized NH_3 yield, and c) ECSA−normalized partial current density of NH_3 for all samples at different potential. The determined ECSA values based on the equation of $ECSA = C_{dl}/Cs \times A$, where C_{dl} is the double−layer capacitance of catalyst, Cs is the capacitance of an atomically smooth planar surface (0.04 mF cm^{-2} in alkaline Media), and A is the electrode geometric area.[14, 15]

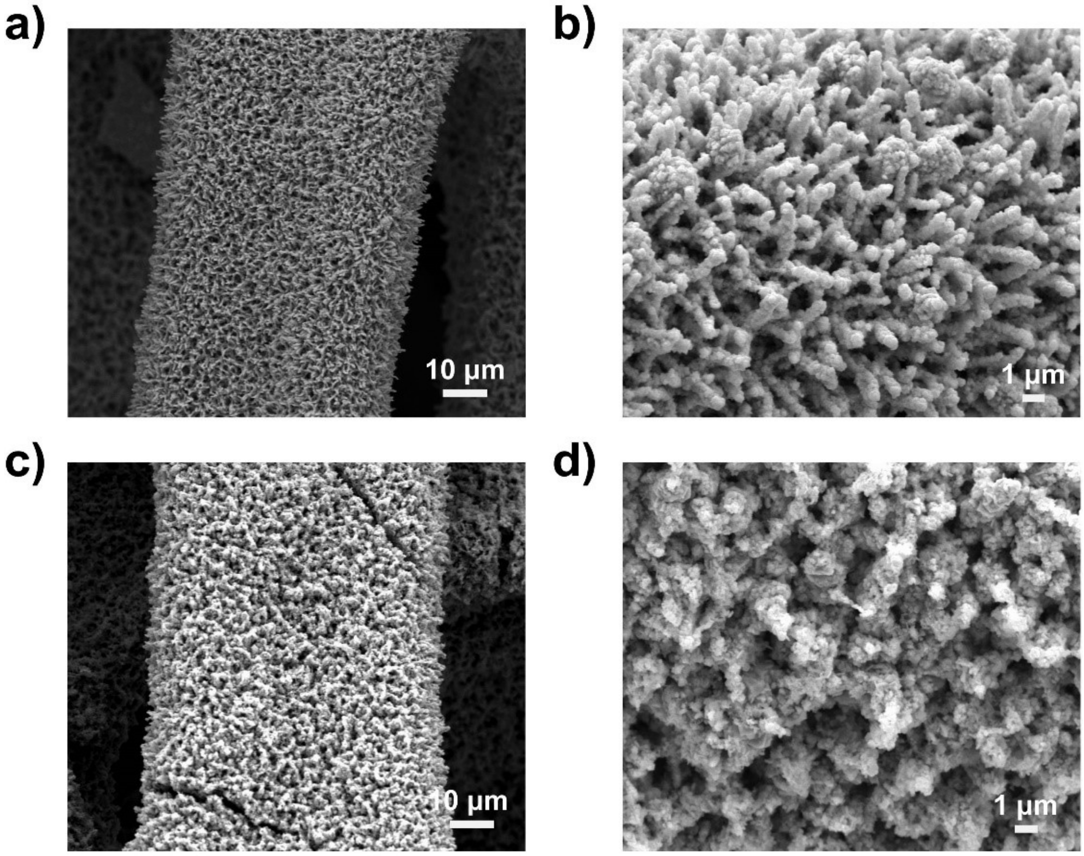

Fig. S40 SEM images of o−CoP/C@Cu_3P/CF after activation and 10th NITRR cycle.

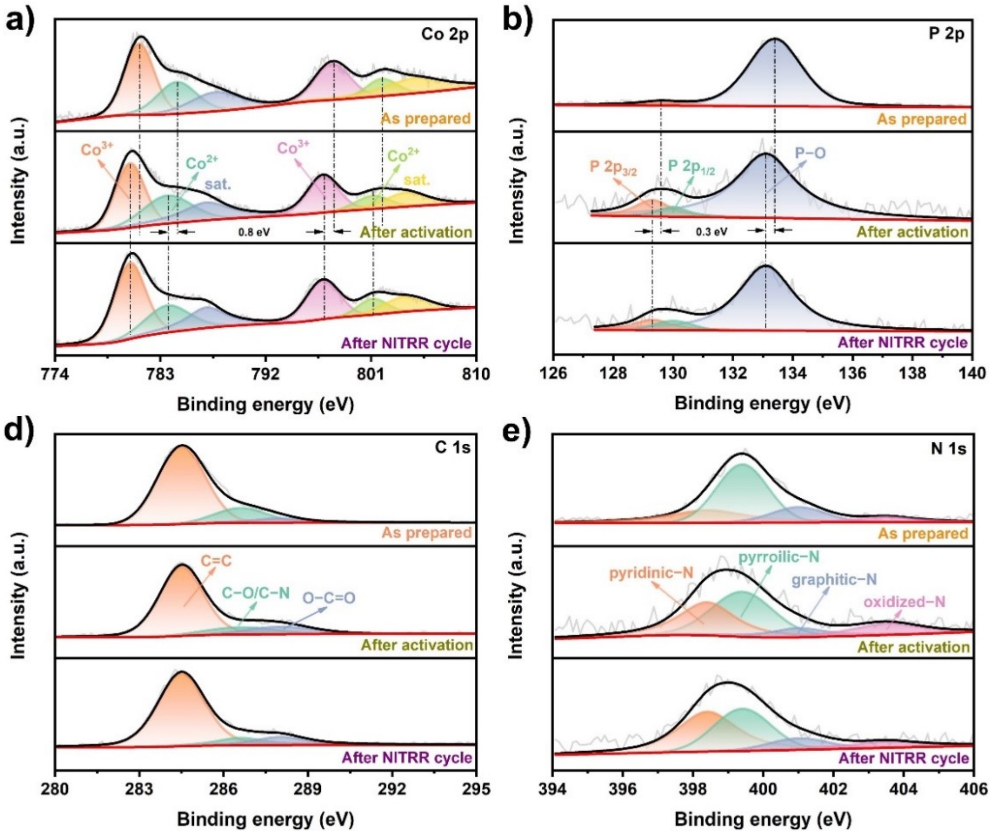

Fig. S41 a) Co 2p, b) P 2p, c) C 1s, and N 1s spectra of o−CoP/C@Cu_3P/CF under different conditions.

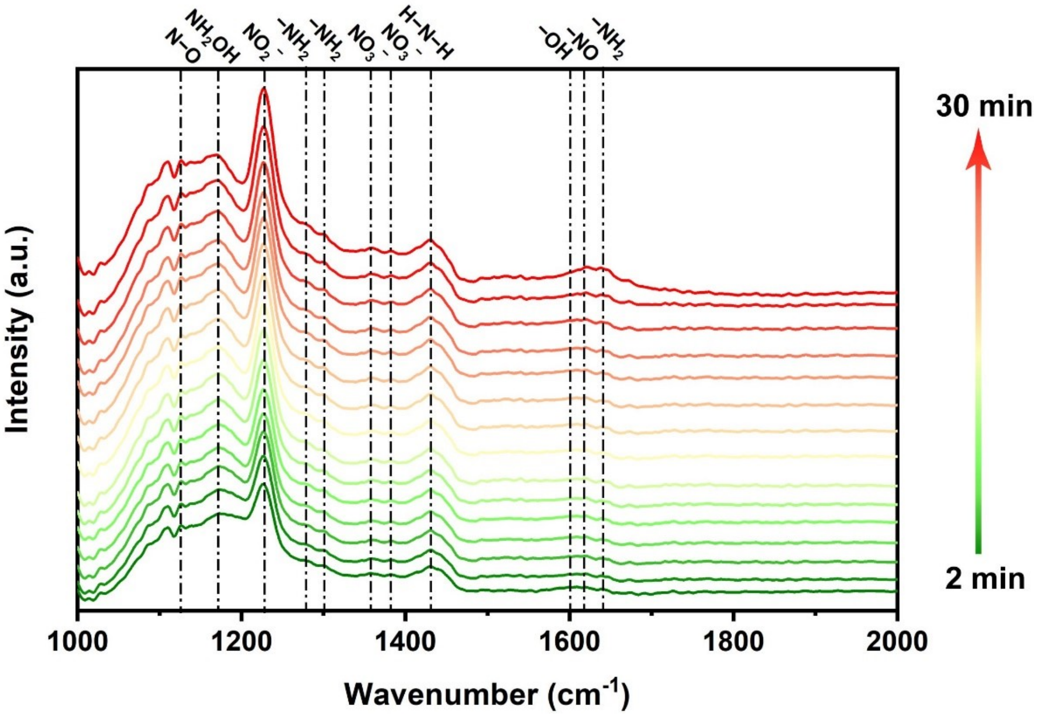

Fig. S42 Time−dependent in situ ATR−SEIRAS of o−CoP/C@Cu_3P at −0.25 V *vs. RHE* during the process of nitrate electrolysis.

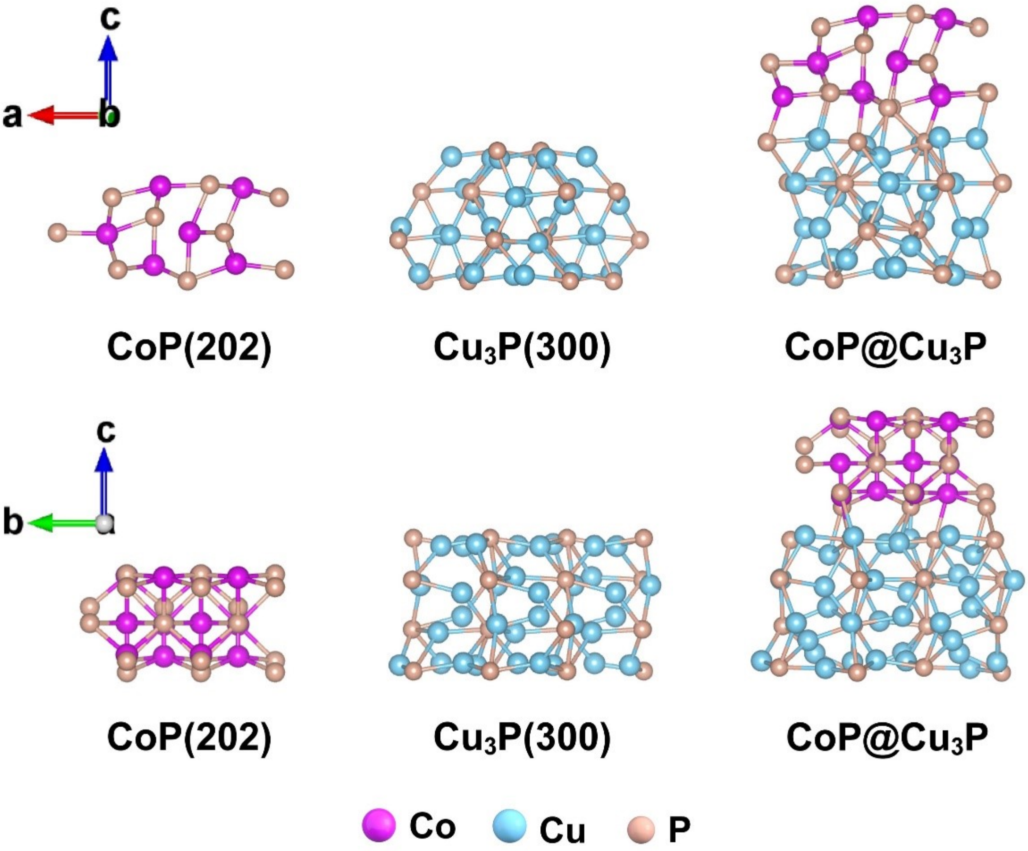

Fig. S43 Optimized structure models of CoP(202), Cu_3P(300) and CoP@Cu_3P.

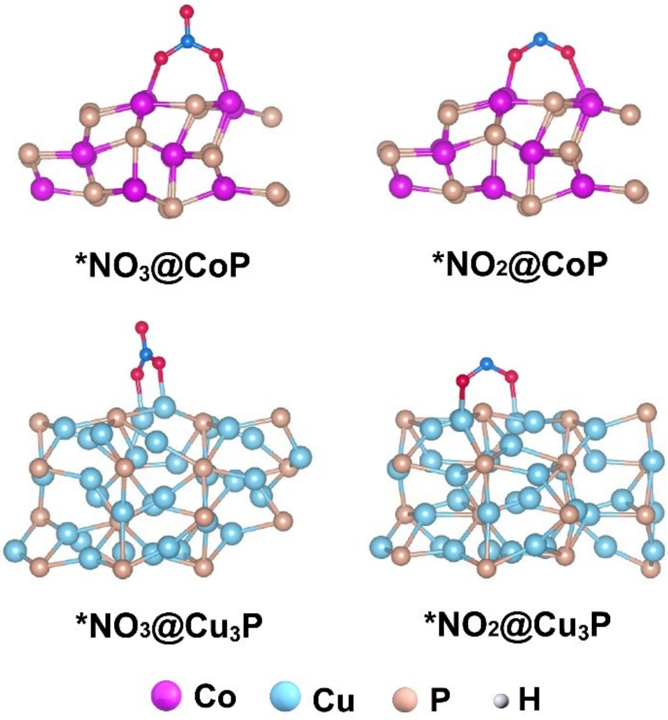

Fig. S44 Optimized structure models of CoP and Cu_3P absorbed with $*NO_3$ and $*NO_2$.

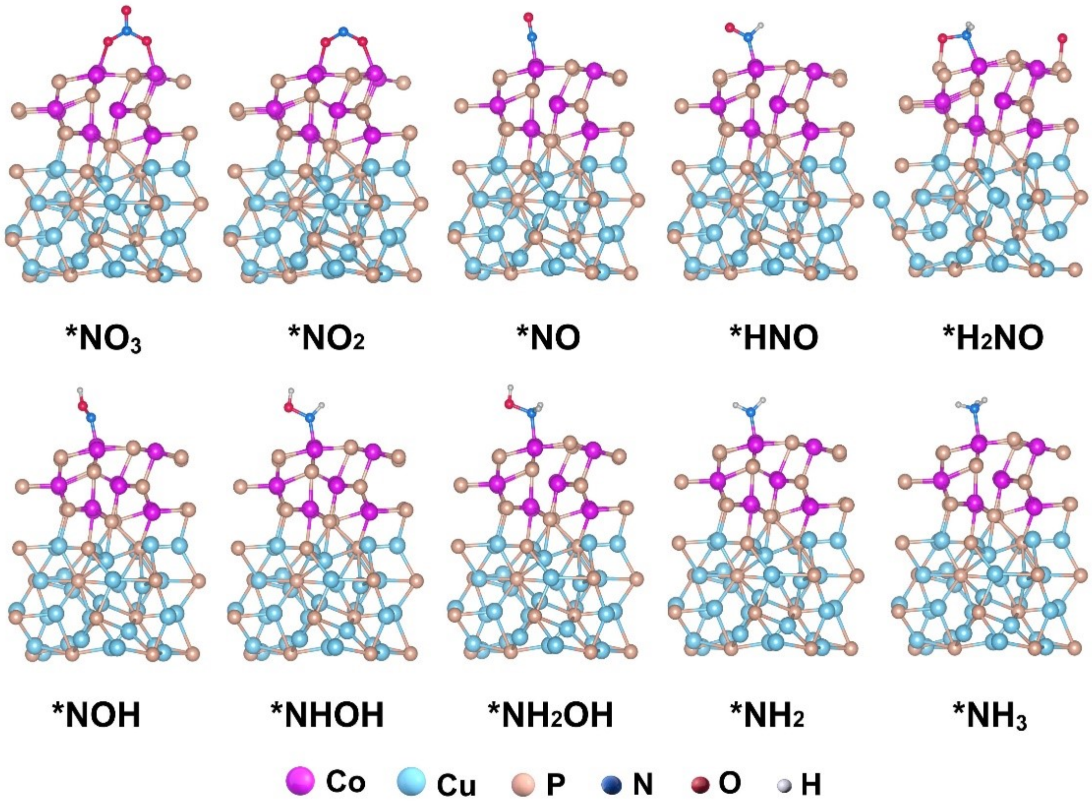

Fig. S45 Optimized structure models of CoP@Cu_3P−Co absorbed with NITRR intermediates.

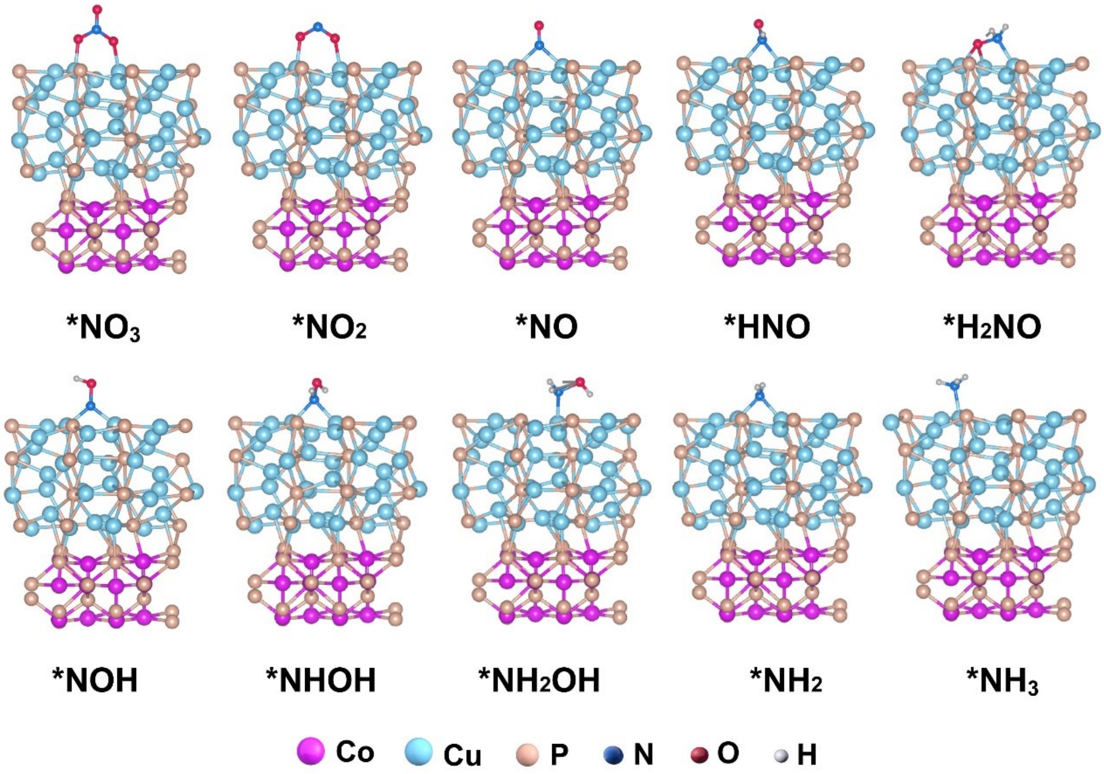

Fig. S46 Optimized structure models of CoP@Cu_3P−Cu absorbed with NITRR intermediates.

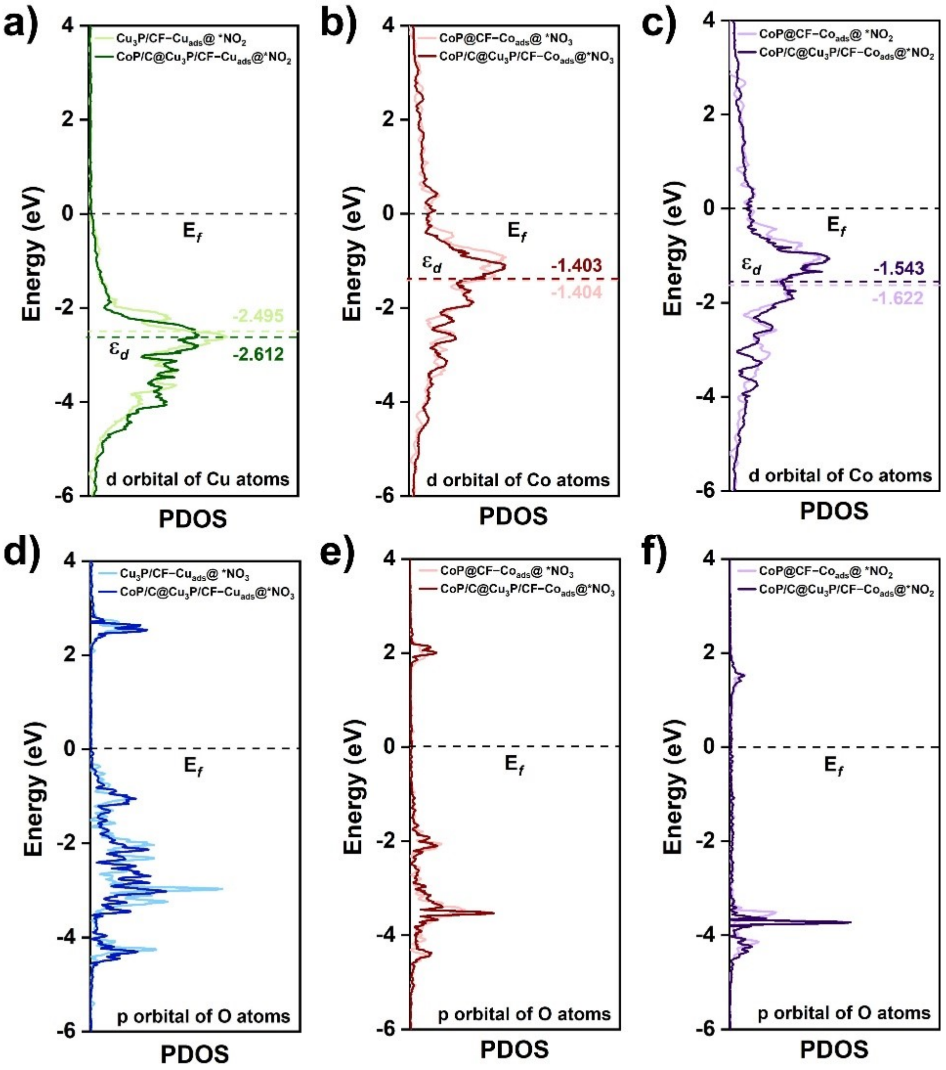

Fig. S47 The PDOS of Cu−d orbital, Co−d orbital, and O−p orbital for active sites adsorbed with $*NO_2$ and $*NO_3$.

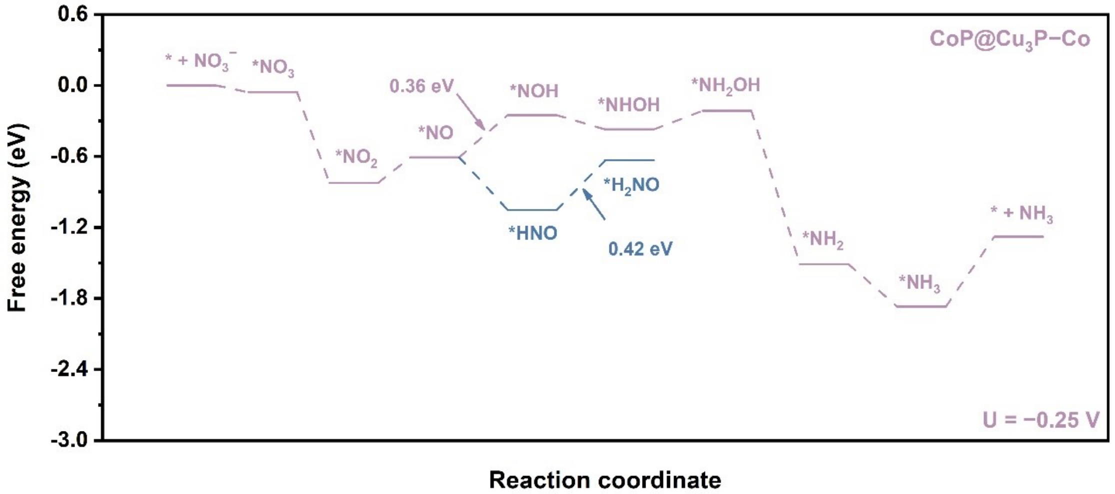

Fig. S48 The Gibbs free energy diagrams of CoP@Cu_3P−Co during nitrate reduction to ammonia process.

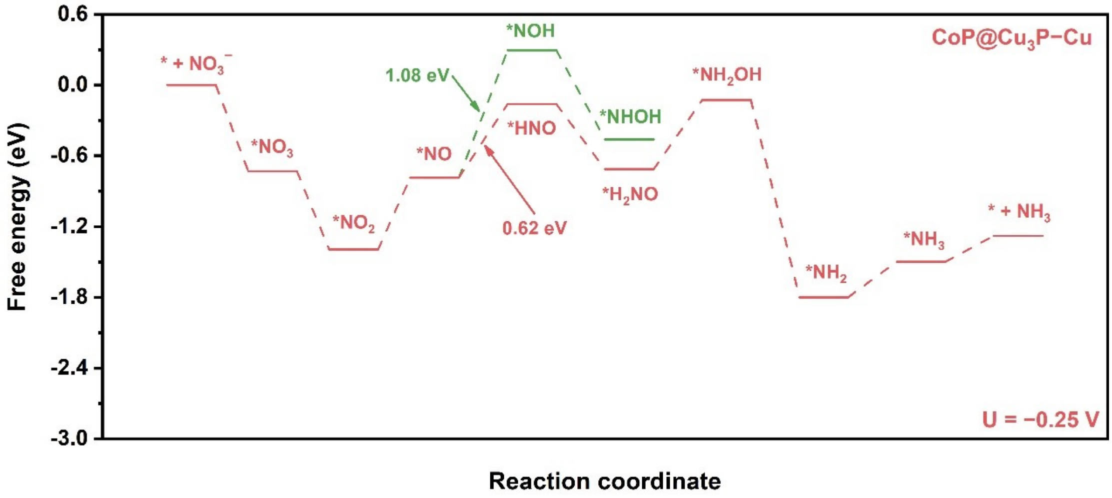

Fig. S49 The Gibbs free energy diagrams of CoP@Cu$_3$P−Cu during nitrate reduction to ammonia process.

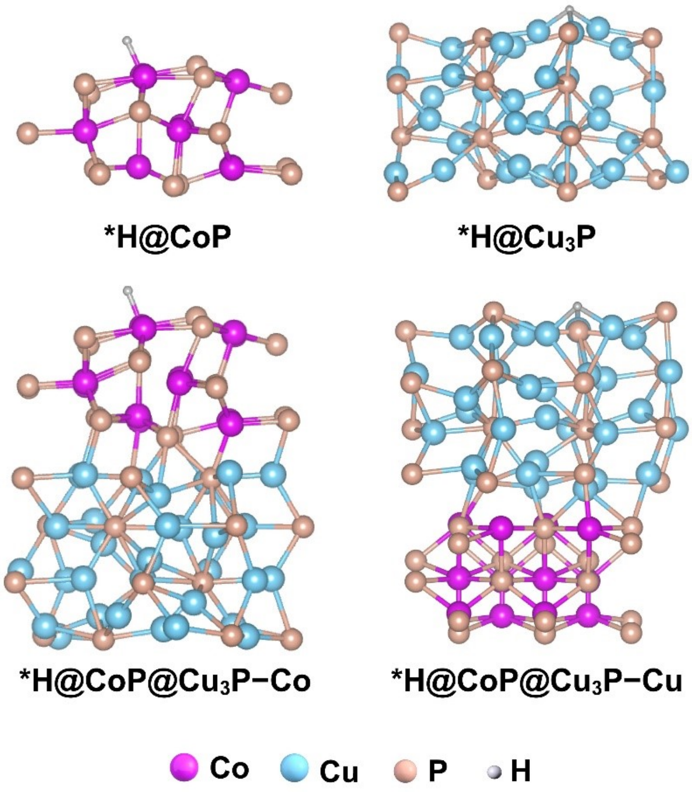

Fig. S50 Optimized structure models of CoP, Cu$_3$P, CoP@Cu$_3$P−Co, and CoP@Cu$_3$P−Cu adsorbed with *H.

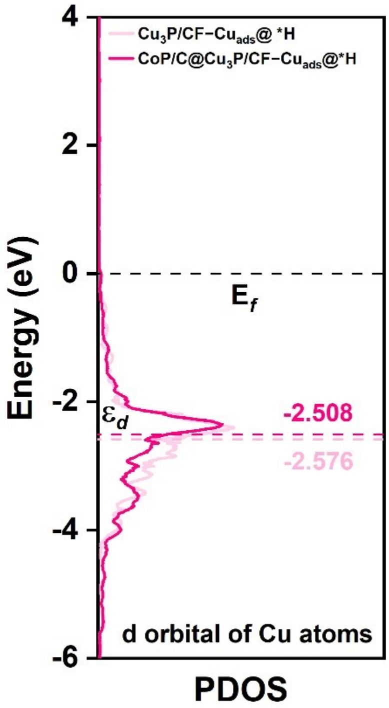

Fig. S51 The PDOS of Cu−d orbital for active sites adsorbed with *H.

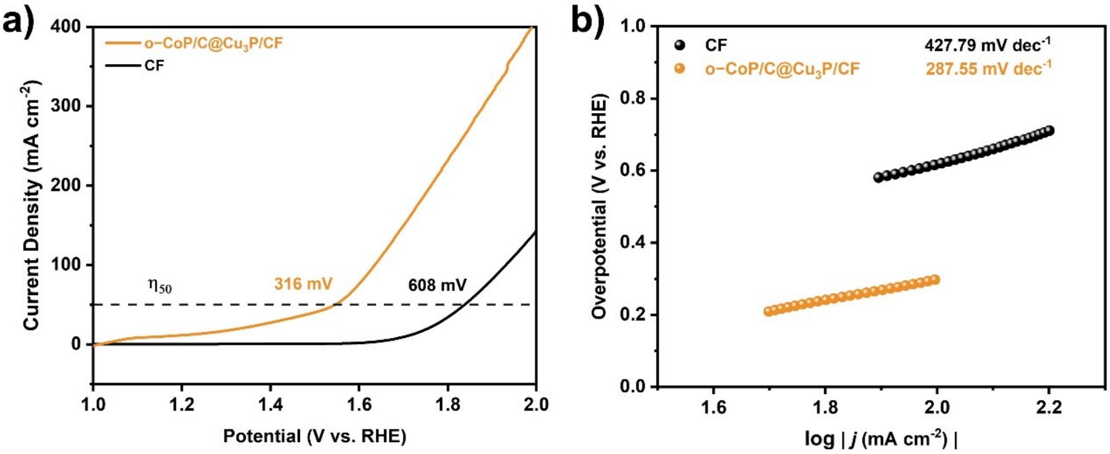

Fig. S52 OER performance. a) LSV polarization curves, b) the corresponding Tafel plots of CF and o−CoP/C@Cu_3P/CF.

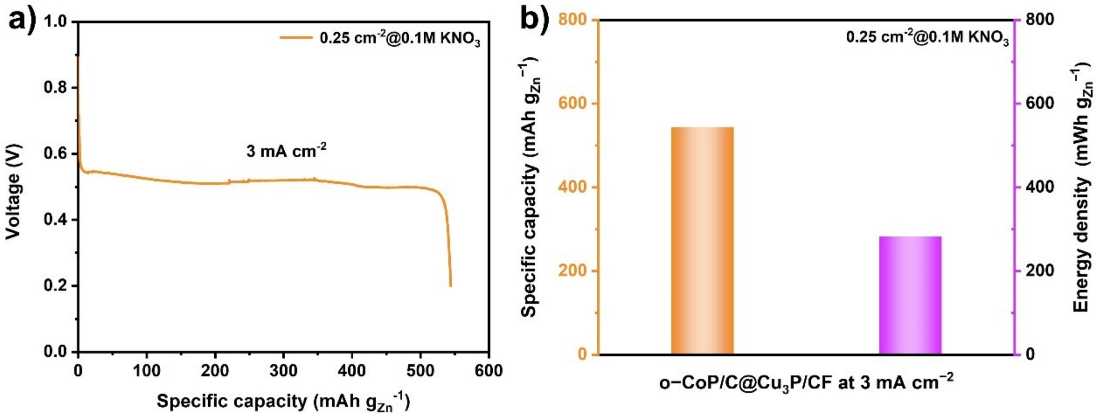

Fig. S53 The specific capacity and the energy density of Zn−NO_3^- battery at 3 mA cm^{-2} based on o−CoP/C@Cu_3P/CF cathode.

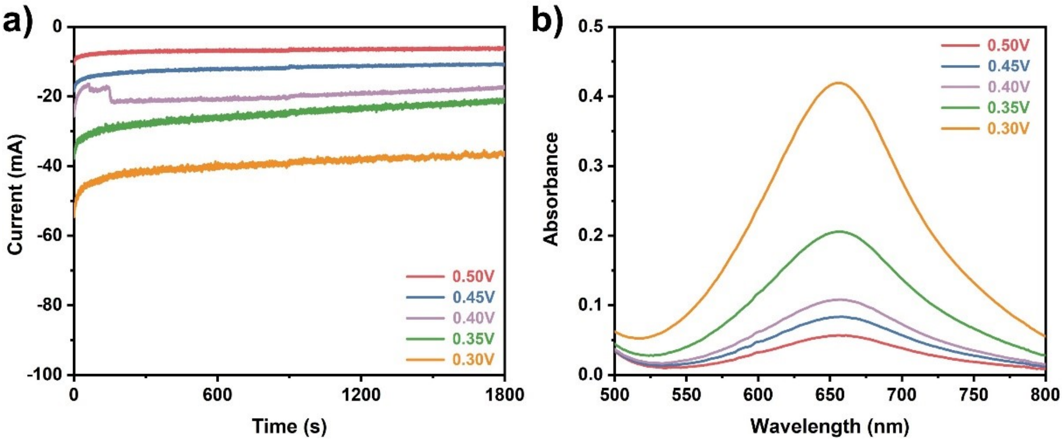

Fig. S54 The NH_3 yield of aqueous Zn−NO_3^- in the process of discharging based on o−CoP/C@Cu_3P/CF. a) CA curves, and b) UV−vis spectrums of the electrolyte (stained with indophenol reagent) after 30 min discharging at different potentials.

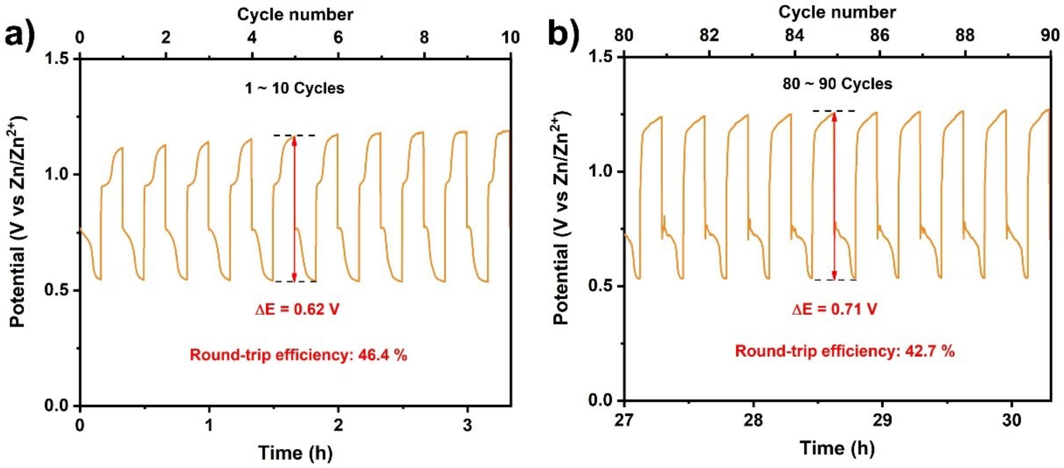

Fig. S55 The discharging–charging cycling stability of Zn−NO_3^- battery at 10 mA cm^{-2} based on o−CoP/C@Cu_3P/CF cathode.

Table S1 ICP−OES of separated o−CoP/C@Cu$_3$P.

Sample	Element	Content (wt %)	Co/Cu (at %)
o−CoP/C@Cu$_3$P	Co	1.360	1.617
	Cu	90.690	

Table S2 Structural parameters of different samples extracted from the EXAFS fitting.

Sample	Shell	CN	R (Å)	σ^2 (10^{-3}Å^2)	ΔE_0 (eV)	R factor
Co foil	Co−Co	12(fixed)	2.50±0.01	3.4±1.6	3.5±1.8	0.002
CoO	Co−O	5.7±0.4	2.10±0.01	9.4±0.7	−2.5±0.7	0.009
	Co−Co	12.7±1.1	3.01±0.01	7.4±0.8		
Co$_3$O$_4$	Co−O	5.1±0.3	1.92±0.01	2.4±0.7	−4.9±1.2	0.003
	Co−Co	4.2±0.7	2.84±0.01	2.7±1.2	−7.9±1.1	
	Co−Co	5.3±1.2	3.35±0.01	8.2±1.5		
o−CoP/C@Cu$_3$P	Co−P	**3.8±1.1**	2.25±0.01	4.6±2.5	−2.5±0.7	0.019
	Co−Co	13.2±0.4	4.05±0.01	7.4±0.8		
CoP	Co−P	**5.8±0.1**	2.25±0.01	3.4±1.9	1.8±2.3	0.017
	Co−Co	12.9±1.2	4.05±0.01	0.5±2.4		

Data ranges: $3.0 \leq k \leq 12.0$ Å^{-1}, $1.0 \leq R \leq 3.5$ Å. R: bond distance; σ^2: Debye−Waller factors; R factor: goodness of fit. S_0^2 is the amplitude reduction factor (S_0^2 =0.74 was obtained by Co foil fitting and applied for the other samples fitting).

Table S3 The BET specific surface area and average pore diameter of ZIF−67$_{\text{powder}}$, CoP$_{\text{powder}}$, and o−CoP/C@Cu$_3$P.

Samples	S_{BET} (m^2/g)	average pore diameter (NLDFT, nm)
ZIF−67$_{\text{powder}}$	1215	1.64
CoP$_{\text{powder}}$	23.25	69.72
o−CoP/C@Cu$_3$P	2.55	37.72

Table S4 Proportion of different elements corresponding to EDS.

Element	Weight %	Atomic %	Uncert. %	Correction	k−Factor
C (K)	18.24	42.93	0,43	0.28	3.601
N (K)	4,25	8.58	0.24	0.28	3.466
P (K)	27.50	25.1	0.28	0.90	1.067
Co (K)	32.44	15.56	0.33	0.99	1.492
Cu (K)	17.54	7.80	0.27	0.99	1.663

Table S5 The NITRR performance of electrocatalysts in previous literature.

Electrocatalyst	**Electrolyte**	**j_{NH3} (mA cm^{-2})**	**FE_{NH3} (%)**	**NH_3 yield (mmol h^{-1} cm^{-2})**	**Ref.**
Cu_3P NA/CF	0.1 M PBS + 0.1 M NO_3^-	~9@−0.6 V *vs. RHE*	62.9 ± 2.0%	0.050 ±0.01	16
$Co_2B@Co_3O_4$/TM	0.1 M PBS + 0.1 M NO_3^-	103.2@−1.0 V *vs. RHE*	~83	0.504	17
Co@TiO_2/TP	0.1 M PBS + 0.1 M NO_3^-	~75@−0.7 V *vs. RHE*	96.7	0.371	18
Rh@Cu−0.6%	0.1 M Na_2SO_4 + 0.1 M NO_3^-	162@−0.2 V *vs. RHE*	93	1.275	19
Fe/Ni_2P	0.2 M K_2SO_4 + 0.05 M NO_3^-	~45@−0.4 V *vs. RHE*	94.3	0.245	20
Co_2NiO_4	0.5 M K_2SO_4 + 0.1 M NO_3^-	~240@−1.0 V *vs. RHE*	94.9	1.176	21
SN Co−Li^+/PCNF	0.5 M Na_2SO_4 + 0.5 M NO_3^-	~165@ H−type cell 528@Flow−cell	72.7 90.2	0.71 2.1	22
Pd/NF	0.5 M Na_2SO_4+ 0.1 M NO_3^-	~500@−1.4 V *vs. RHE*	78 ± 5	1.52 ± 0.15	23
$Cu/Co_{0.85}Se_{VSe}$	0.1 M KOH + 0.01 M NO_3^-	~22@−0.60 V *vs. RHE*	93.5	0.139	11
Cu−RD−KOH	0.1 M KOH + 500 ppm NO_3^-	~40@−0.3 V *vs. RHE*	96.5 ± 1.9%	~0.18	24
CoP/TiO_2@TP	0.1 M NaOH + 0.1 M NO_3^-	~62@−0.3 V *vs. RHE*	95	0.297	25
CuCoSP	0.1 M KOH + 0.1 M NO_3^-	~260@−0.175 V *vs. RHE*	93.3 ± 2.1%	1.17	26
MR Co−NC	0.1 M KOH + 0.1 M NO_3^-	268@−0.7 V *vs. RHE*	95.35 ± 1.75%	1.25 ± 0.023	27
MnCuOx	1 M KOH + 0.1 M NO_3^-	~135@−0.63 V *vs. RHE*	86.4	0.553	28
CoP NAs	1 M NaOH + 1 M NO_3^-	~240@−0.3 V *vs. RHE*	~100	0.956	29
CuCo−TPA−E	1 M KOH + 0.1 M NO_3^-	~170@−0.326 V *vs. RHE*	99.62	1.12	30
RuOx/Pd	1 M KOH + 0.1 M NO_3^-	296@−0.5 V *vs. RHE*	98.6	1.382	31
Bi−Cl_{red}	1 M KOH + 0.5 M NO_3^-	300@−0.5 V *vs. RHE*	75	1.395	14
FeB_2	1 M KOH + 0.1 M NO_3^-	321.6@−0.6 V *vs. RHE*	96.8	1.5	32
This work	**1 M KOH + 0.05 M NO_3^-**	**352@−0.25 V *vs. RHE***	**96.23±0.55**	**1.649±0.009**	

Table S6 The Zn−NO_3^- battery performance of electrode in previous literatures.

Battery	Electrolyte	Cathode	OCV (V vs. Zn/Zn^{2+})	Power density (mW cm^{-2})	NH_3 yield (mg h^{-1} cm^{-2})	Ref.
Zn−NO_3^-	0.5 M Na_2SO_4 + 5 mM NO_3^-	CoNi−Vp−1.0	1.03	1.05	0.21	33
Zn−NO_3^-	0.2 M K_2SO_4 + 0.05 M NO_3^-	Fe/Ni_2P	1.22	3.25	0.384	20
Zn−NO_3^-	5 M LiCl + 0.25 M NO_3^-	Pd/TiO_2	0.81	0.87	0.54	34
Zn−NO_3^-	1 M KOH+1 M NO_3^-	DM−Co	0.62	25.8	2.04	35
Zn−NO_3^-	1 M KOH + 0.1 M NO_3^-	0.6W−O−CoP	0.7	9.27	2.79	36
Zn−NO_3^-	1 M KOH + 1M NO_3^-	Ru−25CV/NF	1.2	51.5 (0.25 cm^2) 23.3 (1.0 cm^2)	2.9	37
Zn−NO_3^-	1 M KOH + 0.1 M NO_3^-	CuCo−TPA−E	1.32	8.46	3.79	30
Zn−NO_3^-	3M KOH+0.5 M NO_3^-	Cu−RD−KOH	0.943	14.1		24
Zn−NO_2^-	3M KOH+ 0.5M NO_2^-		0.939	9.15	~3.25	
Zn−NO_2^-	0.5 M K_2SO_4 +50 mM NO_2^-	C/Co_3O_4	1.45	6.03	~1.15	38
This work	**1 M KOH + 1 M NO_3^-**	**o−CoP/C @Cu_3P/CF**	**0.82**	**58.0 (0.25 cm^2)**		
	1 M KOH + 0.1 M NO_3^-		**0.78**	**40.1 (0.25 cm^2)** **23.1 (1.0 cm^2)**	**4.42**	

3. Supplementary references

1. O. Peng, Q. Hu, X. Zhou, R. Zhang, Y. Du, M. Li, L. Ma, S. Xi, W. Fu, Z.−X. Xu, C. Cheng, Z. Chen and K. P. Loh, *ACS Catal.,* **2022**, 12, 15045−15055.
2. Z. Jiang, Y. Wang, Z. Lin, Y. Yuan, X. Zhang, Y. Tang, H. Wang, H. Li, C. Jin and Y. Liang, *Energy Environ. Sci.,* **2023**, 16, 2239−2246.
3. Y. Li, Y. Liang, H. Li, B. Wang, H. You, Y. Wang, Y. Cao, W. Dai and F. Gao, *Appl. Surf. Sci.,* **2021**, 570,151257.
4. J. P. Perdew, K. Burke and M. Ernzerhof, *Phys. Rev. Lett.,* **1996**, 77, 3865−3868.
5. J. P. Perdew, M. Ernzerhof and K. Burke, The *J. Chem. Phys.,* **1996**, 105, 9982−9985.
6. G. Kresse and J. Furthmüller, Physical Review B, *Phys. Rev. B,* **1996**, 54, 11169−11186.
7. G. Kresse and J. Furthmüller, *Computational Materials Science,* **1996**, 6, 15−50.
8. S. Grimme, *J Comput Chem,* **2006**, 27, 1787−1799.
9. P. E. Blöchl, *Phys. Rev. B,* **1994**, 50, 17953−17979.
10. V. Wang, N. Xu, J.−C. Liu, G. Tang and W.−T. Geng, *Comput Phys Commun,* **2021**, 267, 108033.
11. Z. Gu, Y. Zhang, X. Wei, Z. Duan, Q. Gong and K. Luo, *Adv. Mater.,* **2023**, 35, 2303107.
12. Y. Fu, S. Wang, Y. Wang, P. Wei, J. Shao, T. Liu, G. Wang and X. Bao, *Angew.Chem. Int. Ed.,* **2023**, 62, e202303327.
13. F. Calle−Vallejo, M. Huang, J. B. Henry, M. T. M. Koper and A. S. Bandarenka, *Phys. Chem. Chem. Phys.,* **2013**, 15, 3196−3202.
14. N. Zhang, J. Shang, X. Deng, L. Cai, R. Long, Y. Xiong and Y. Chai, *ACS Nano,* **2022**, 16, 4795−4804.
15. C. C. L. McCrory, S. Jung, J. C. Peters and T. F. Jaramillo, *J. Am. Chem. Soc.,* **2013**, 135, 16977−16987.
16. J. Liang, B. Deng, Q. Liu, G. Wen, Q. Liu, T. Li, Y. Luo, A. A. Alshehri, K. A. Alzahrani, D. Ma and X. Sun, *Green Chem.,* **2021**, 23, 5487−5493.
17. L. Xie, S. Sun, L. Hu, J. Chen, J. Li, L. Ouyang, Y. Luo, A. A. Alshehri, Q. Kong, Q. Liu and X. Sun, *ACS Appl. Mater. Interfaces,* **2022**, 14, 49650−49657.
18. X. Fan, D. Zhao, Z. Deng, L. Zhang, J. Li, Z. Li, S. Sun, Y. Luo, D. Zheng, Y. Wang, B. Ying, J. Zhang, A. A. Alshehri, Y. Lin, C. Tang, X. Sun and Y. Zheng, *Small,* **2023**, 19, 2208036.
19. H. Liu, X. Lang, C. Zhu, J. Timoshenko, M. Rüscher, L. Bai, N. Guijarro, H. Yin, Y. Peng, J. Li, Z. Liu, W. Wang, B. R. Cuenya and J. Luo, *Angew.Chem. Int. Ed.,* **2022**, 61, e202202556.
20. R. Zhang, Y. Guo, S. Zhang, D. Chen, Y. Zhao, Z. Huang, L. Ma, P. Li, Q. Yang, G. Liang and C. Zhi, *Adv. Energy Mater.,* **2022**, 12, 2103872.
21. L. Qiao, D. Liu, A. Zhu, J. Feng, P. Zhou, C. Liu, K. W. Ng and H. Pan, *Appl. Catal. B,* **2024**, 340, 123219.
22. L. Mi, Q. Huo, J. Cao, X. Chen, H. Yang, Q. Hu and C. He, *Adv. Energy Mater.,* **2022**, 12, 2202247.
23. H. Guo, M. Li, Y. Yang, R. Luo, W. Liu, F. Zhang, C. Tang, G. Yang and Y. Zhou, *Small,* **2023**, 19, 2207743.

24. H. Jiang, G. F. Chen, O. Savateev, J. Xue, L. X. Ding, Z. Liang, M. Antonietti and H. Wang, *Angew.Chem. Int. Ed.,* **2023**, 62, e202218717.
25. Z. Deng, C. Ma, X. Fan, Z. Li, Y. Luo, S. Sun, D. Zheng, Q. Liu, J. Du, Q. Lu, B. Zheng and X. Sun, *Mater. Today Phys.,* **2022**, 28, 100854.
26. W. He, J. Zhang, S. Dieckhöfer, S. Varhade, A. C. Brix, A. Lielpetere, S. Seisel, J. R. C. Junqueira and W. Schuhmann, *Nat. Commun.,* **2022**, 13, 1129.
27. S. Xu, Y. Shi, Z. Wen, X. Liu, Y. Zhu, G. Liu, H. Gao, L. Sun and F. Li, *Appl. Catal. B,* **2023**, 323, 122192.
28. D. Jang, J. Maeng, J. Kim, H. Han, G. H. Park, J. Ha, D. Shin, Y. J. Hwang and W. B. Kim, *Appl. Surf. Sci.,* **2023**, 610, 155521.
29. S. Ye, Z. Chen, G. Zhang, W. Chen, C. Peng, X. Yang, L. Zheng, Y. Li, X. Ren, H. Cao, D. Xue, J. Qiu, Q. Zhang and J. Liu, *Energy Environ. Sci.,* **2022**, 15, 760−770.
30. J. Yang, W.−D. Zhang, H. Zhao, Y. Zou, Z.−Y. Zhang, J. Liu, J. Wang, Z.−G. Gu and X. Yan, *Appl. Catal. B,* **2024**, 340, 123237.
31. X. Li, P. Shen, X. Li, D. Ma and K. Chu, *ACS Nano,* **2023**, 17, 1081−1090.
32. G. Zhang, X. Li, K. Chen, Y. Guo, D. Ma and K. Chu, *Angew.Chem. Int. Ed.,* **2023**, 62, e202300054.
33. Y. Gao, K. Wang, C. Xu, H. Fang, H. Yu, H. Zhang, S. Li, C. Li and F. Huang, *Appl. Catal. B,* **2023**, 330, 122627.
34. Y. Guo, R. Zhang, S. Zhang, Y. Zhao, Q. Yang, Z. Huang, B. Dong and C. Zhi, *Energy Environ. Sci.,* **2021**, 14, 3938−3944.
35. W. Lin, E. Zhou, J. F. Xie, J. Lin and Y. Wang, *Adv. Funct. Mater.,* **2022**, *32*, 2209464.
36. Z. Chang, G. Meng, Y. Chen, C. Chen, S. Han, P. Wu, L. Zhu, H. Tian, F. Kong, M. Wang, X. Cui and J. Shi, *Adv. Mater.,* **2023**, 35, 2304508.
37. F. Zhou and C. Sun, *Small,* **2022**, 18, e2200436.
38. R. Zhang, S. Zhang, Y. Guo, C. Li, J. Liu, Z. Huang, Y. Zhao, Y. Li and C. Zhi, *Energy Environ. Sci.,* **2022**, 15, 3024−3032.